CE-STR-80-12

PLASTICITY MODELS FOR SOILS
PART I: THEORY AND CALIBRATION
PART II: COMPARISON AND DISCUSSION

by E. Mizuno and W. F. Chen

Presented at the May 28-30, 1980 North American Workshop on Limit Equilibrium, Plasticity and Generalized Stress-Strain in Geotechnical Engineering - Jointly Sponsored by NSF/NSERC.

This material is based upon work supported by the National Science Foundation under Grant No. PFR-7809326 to Purdue University.

School of Civil Engineering
Purdue University
West Lafayette, IN 47907

July, 1980

50272-101

REPORT DOCUMENTATION PAGE	1. REPORT NO. NSF/RA-800208	2.	3. Recipient's Accession No. PB81 120065
4. Title and Subtitle: Plasticity Models for Soils, Part I: Theory and Calibration; Part II: Comparison and Discussion			5. Report Date: July 1980 6.
7. Author(s): E. Mizuno, W. F. Chen			8. Performing Organization Rept. No. CE-STR-80-12
9. Performing Organization Name and Address: Purdue University School of Civil Engineering West Lafayette, IN 47907			10. Project/Task/Work Unit No. 11. Contract(C) or Grant(G) No. (C) (G) PFR7809326
12. Sponsoring Organization Name and Address: Engineering and Applied Science (EAS) National Science Foundation 1800 G Street, N.W. Washington, D.C. 20550			13. Type of Report & Period Covered 14.

15. Supplementary Notes

16. Abstract (Limit: 200 words)

Three types of soil models are described in this report: (1) nonlinear elasticity material model with the Mohr-Coulomb or the Drucker-Prager surface as failure criterion; (2) Mohr-Coulomb type of elastic-plastic material model with two different sizes of elliptical hardening cap which are defined respectively on the tensile meridian plane and the compressive meridian plane; (3) Mohr-Coulomb type of elastic-plastic material model with an elliptical hardening cap whose size depends on the Lode angle theta. The following assumptions are made for the three types of models: (1) the linear elastic, hypoelastic or hyperelastic function is used in the elastic range for the isotropic or anisotropic material element; (2) the incremental plasticity theory is applied to calculate plastic strain increment during loading range. The concept of "decomposition" of stress state onto tensile meridian plane and compressive meridian plane is described.

17. Document Analysis a. Descriptors

Soils
Models
Plastic properties
Elastic properties
Tensile properties
Soil mechanics

b. Identifiers/Open-Ended Terms

Earthquake Hazards Mitigation

c. COSATI Field/Group

18. Availability Statement	19. Security Class (This Report)	21. No. of Pages
NTIS	20. Security Class (This Page)	22. Price

(See ANSI-Z39.18) See Instructions on Reverse

OPTIONAL FORM 272 (4-77)
(Formerly NTIS-35)
Department of Commerce

PLASTICITY MODELS FOR SOILS

Theory and Calibration

by

E. Mizuno[1] and W. F. Chen[2], M. ASCE

1. Introduction

The mechanical behavior of soil and rock is complicated and they can not be modelled accurately as a continuum. At present, however, the concept of continuum mechanics has been used extensively in the mathematical modelling of these materials. These include the applications of linear elastic models, nonlinear elastic models, and elastic-plastic models to geotechnical engineering problems. Although the models such as hyperelastic or hypoelastic can represent the phenomena such as dilitancy and hardening or softening of soil behavior, the effect of plastic strain induced during loading can not be predicted within the framework of an incremental Hooke's law with variable moduli which are functions of the stress and/or strain levels.

Current research in soil constitutive modelling is moving toward the development of three-dimensional stress-strain relations based on the principles of plasticity as well as elasticity.

Herein, three types of soil models are described. The first type was used for prediction before the workshop was held, thus without the benefit of the test results. The second and third types are subsequently developed and used after the workshop.

(i) Nonlinear elasticity material model with the Mohr-Coulomb or the Drucker-Prager surface as failure criterion.

(ii) Mohr-Coulomb type of elastic-plastic material model with two different sizes of elliptical hardening cap which are defined respectively on the tensile meridian plane ($\theta = 0°$) and the compressive meridian plane ($\theta = 60°$). (Cap Model I)

[1]Research Assistant, School of Civil Engineering, Purdue University, West Lafayette, IN 47907

[2]Professor of Structural Engineering, School of Civil Engineering, Purdue University, West Lafayette, IN 47907

(iii) Mohr-Coulomb type of elastic-plastic material model with an elliptical hardening cap whose size depends on the Lode angle θ. (Cap Model II).

2. A Brief Historical Review

The Mohr-Coulomb criterion of failure is certainly the best known in soil mechanics. This criterion states that failure occurs when the shear stress τ and the normal stress σ acting on any element in the material satisfy the linear equation.

$$\tau + \sigma \tan \phi - c = 0 \tag{1}$$

where c and ϕ denote the cohesion and the angle of internal friction, respectively.

Although this criterion has in the past been used by necessity and simplicity to obtain reasonable solutions to important, practical problems in geotechnical engineering, the following limitations should be noticed: (1) This criterion neglects the influence of intermediate principal stress on shear strength; and (2) the failure surface of the Mohr-Coulomb criterion exhibits corners or singularities in the three dimensional principal stress space. From the second limitation, these singularities are difficult to handle in a numerical analysis.

The Drucker-Prager surface [7] can then be considered as a three dimensional approximation to the Mohr-Coulomb failure criterion with a simple smooth surface. This criterion is expressed as a linear combination of the first invariant of stress tensor I_1 and the square root of the second invariant of the deviatoric stress tensor $\sqrt{J_2}$ together with two material constants α and k. The material constants α, k can be related to the Coulomb's c and ϕ constants in several ways. The Drucker-Prager yield surface with an associated flow rule, however, can not predict the plastic volumetric strain observed in experiments. To improve this, extended von Mises model with convex end cap was proposed by Drucker, Gibson and Kenkel [6].

Following the concept of Drucker et al., subsequent strain hardening plasticity models using the critical state concept were developed by researchers at Cambridge [12], and a specific Cam-Clay model based on normally consolidated or lightly overconsolidated clay was suggested by Roscoe,

Schofield, and Thurairajah [9]. However, failure surface used in this model is still the Drucker-Prager type which resultsin a much greater dilatancy prediction than that observed in experiments. As a result, modified failure or yield criterion with an elliptical hardening cap which controls the dilatancy was subsequently proposed by DiMaggio and Sandler [5]. In recent years, the cap model has been further modified and refined by Sandler [10,11] and Baladi [1]. Various advanced version of this model including such features as kinematic hardening, double hardening etc. have recently been proposed. The historical review of the plasticity modelling of geotechnical materials has been given in a recent paper by Chen [3].

3. Notations

The state of stress at a point inside a soil medium can be completely determined by the stress tensor σ_{ij} in a three dimensional space. In general, the stress tensor can be decomposed into two parts: (1) the hydrostatic pressure part, where the off-diagonal terms are identically zeros and the diagonal terms are equal to mean normal stress; and (2) the deviatoric part S_{ij}. Thus,

$$\sigma_{ij} = \frac{1}{3} I_1 \delta_{ij} + S_{ij} \tag{2}$$

where I_1, the first invariant of the stress tensor, is the sum of the diagonal stress componsnts and δ_{ij} is the Kronecker delta. The hydrostatic pressure and the deviatoric stress, respectively, cause volumetric change and shape change of the material element.

Fig. 1 shows the view of the state of stress in the principal stress coordinate system (σ_1, σ_2, σ_3). Stress vector $\overrightarrow{OA}$ can be decomposed into $\overrightarrow{OB}$ in the ξ-axis which is called hydrostatic axis ($\sigma_1 = \sigma_2 = \sigma_3$) and $\overrightarrow{BA}$ in the deviatoric plane (π-plane) which is perpendicular to the ξ-axis. The component vector $\overrightarrow{OB}$ represents the mean normal stress p ($I_1/3$) and the component $\overrightarrow{BA}$ represents the deviatoric stress S_{ij}. The length of $\overrightarrow{OB}$ and $\overrightarrow{BA}$ are $\sqrt{3}$ p and $\rho = \sqrt{S_{11}^2 + S_{22}^2 + S_{33}^2}$, respectively. If the stress vector $\overrightarrow{OA}$ is viewed from the hydrostatic ξ-axis, the actual length and direction of it can be represented respectively by ρ and the Lode angle θ. The Lode angle θ is given by

$$\theta = \frac{1}{3} \cos^{-1} \left(\frac{3\sqrt{3}}{2} \frac{J_3}{J_2^{3/2}}\right) \tag{3}$$

where J_3 is the third invariant of the deviatoric stress tensor.

In this paper, the typical continuum mechanics sign convention (tensile stress positive) is utilized in the theoretical development.

4. Failure and Yield Functions

The following failure and yield functions are used in the three proposed models to be described in the subsequent sections.

Mohr-Coulomb Criterion

The Mohr-Coulomb criterion given by Eq. 1 can now be written more generally in terms of stress invariants [8,14].

$$F = I_1 \sin\phi + \frac{3(1-\sin\phi) \sin\theta + \sqrt{3}(3+\sin\phi) \cos\theta}{2} \sqrt{J_2} - 3c \cos\phi = 0 \tag{4}$$

where θ is the Lode angle (Eq. 3).

The cross sectional shape of the Mohr-Coulomb surface on the deviatoric plane is an irregular hexagon as shown in Fig. 2.

Drucker-Prager Criterion

This criterion has the simple form:

$$F = \alpha I_1 + \sqrt{J_2} - k = 0 \tag{5}$$

where α and k are material constants which can be related to cohesion c and the angle of internal friction ϕ of the Mohr-Coulomb criterion in several ways. For example, if the Drucker-Prager criterion is matched with the Mohr-Coulomb criterion in three dimensional principal stress space (Fig. 2) along the compressive meridian (point A) or tensile meridian (point B), the two sets of familiar material constants α and k can be obtained. For the compressive meridian matching, substituting $\theta = \pi/3$ into Eq. 4 and rearranging it, we obtain

$$\left.\begin{aligned} \alpha &= \frac{2 \sin \phi}{\sqrt{3}\ (3-\sin \phi)} \\ k &= \frac{6c \cos \phi}{\sqrt{3}\ (3-\sin \phi)} \end{aligned}\right\} \qquad (6)$$

These material constants are identical to those given by Zienkiewicz [13]. For the tensile meridian matching, substituting $\theta = 0°$ in Eq. 4 and we obtain

$$\left.\begin{aligned} \alpha &= \frac{2 \sin \phi}{\sqrt{3}\ (3+\sin \phi)} \\ k &= \frac{6c \cos \phi}{\sqrt{3}\ (3+\sin \phi)} \end{aligned}\right\} \qquad (7)$$

Various matchings between the Drucker-Prager surface and the Mohr-Coulomb surface for material constants are given by Chen and Mizuno [4]. In general, if α is zero, Eq. 5 reduces to the well known von Mises yield condition for metals. The Drucker-Prager surface is used here as the failure surface for cap models described in what follows. Eq. 5 represents an axisymmetric cone-shaped surface with respect to $\sigma_1 = \sigma_2 = \sigma_3$ axis in principal stress space (Fig. 2).

5. Conventional Cap Models

The loading functions are usually assumed to be isotropic and to consist of the following three parts:

(i) An ultimate failure envelope can be either of the simple linear Drucker-Prager form or the nonlinear form assumed by Sandler [11].

$$F_L = \sqrt{J_2} - (A - C e^{BI_1}) \qquad (8)$$

in which A, B and C are material constants. Here, the failure equation becomes parallel to I_1 axis under large value of I_1, and this results in a limited dilatancy under high pressure I_1.

(ii) Strain-hardening cap function has the form of a quarter of an ellipse (Fig. 3)

$$F_c = F_c(I_1, \sqrt{J_2}, \varepsilon_{kk}^P) = (I_1-L)^2 + R^2 J_2 - (x-L)^2 = 0 \tag{9}$$

in which x is the intersection of cap with I_1 axis and x is also a hardening function which depends on plastic volumetric change $d\varepsilon_{kk}^P$. The location of the cap x is related to the plastic volumetric strain function ε_{kk}^P with the material constants W and D according to

$$\varepsilon_{kk}^P = W(e^{Dx} - 1) \tag{10}$$

and R is the ratio of the major to the minor axis of the cap ellipse which may be a function of L and the Lode angle θ, and L is the value of I_1 at the center of the elliptic cap; and

(iii) Tension cutoff limit plane is introduced

$$F_t = I_1 - T = 0 \tag{11}$$

where T is tension cutoff limit.

The cap can control the dilatancy of soils under hydrostatic pressure I_1. Although the cap can predict not only strain-hardening of soils, but also strain-softening, this type of model can not predict exactly the hysteresis loop under shear loading. This is because the hardening function in this model is assumed to be controlled by plastic volumetric strain.

Each of these models mentioned above contains several material constants which can be determined from data of standard simple shear test, isotropic consolidation test, uniaxial strain test, and triaxial compression, tension tests.

The determination of these material constants will be given in the part on model calibration.

6. Basic Concepts of Models Developments

The following assumptions are made for the three types of models considered here [2]

(i) Linear elastic, hypoelastic or hyperelastic function is used in the elastic range for the isotropic or anisotropic material element,

(ii) Incremental plasticity theory is applied to calculate plastic strain increment during loading range,

(iii) The Mohr-Coulomb or the Drucker-Prager criterion is used as failure criterion. Effect of strain hardening on this portion of surface is not considered,

(iv) Associated flow rule is assumed for the cap hardening portion of the surface.

$$d\varepsilon_{ij}^{P} = d\lambda \frac{\partial F_c}{\partial \sigma_{ij}} \tag{12}$$

where $d\lambda$ is positive scalar function.

In the following, the concept of "decomposition" of stress state onto tensile meridian plane and compressive meridian plane is described.

Suppose that σ_{ij} is the principal stress state acting on an element in soil mass and $d\sigma_{ij}$ is the principal stress increment after the application of an external load increment. The representation of the state of stress as viewed in $I_1 - \sqrt{J_2}$ space is shown in Fig. 4. The CTE line in Fig. 4 is on the $\theta = 0°$ plane and represents the conventional triaxial extension test. The CTC line is on the $\theta = 60°$ plane and represents the conventional triaxial compression test. If stress path is along I_1 axis, it represents the isotropic consolidation test. These three tests are commonly performed tests in geotechnical field. The strengths obtained by the compression test and tension test for soils are different, and the bulk moduli K and shear moduli G determined from these tests are also different. Thus, in the proposed modelling, different material constants (bulk modulus K and shear modulus G) for CTE and CTC tests are introduced. The following items are taken into consideration in the present developments.

(i) The state of stress σ_{ij} as represented in $I_1 - \sqrt{J_2}$ space lies in the range of Lode angle from $\theta = 0°$ and $\theta = 60°$.

(ii) The behaviors of material corresponding to the paths lying on the tensile and compressive meridian planes ($\theta = 0°$ and $\theta = 60°$) are determined first from CTE and CTC tests, respectively.

(iii) The behavior of material corresponding to a stress path lying on a plane making an angle $0° \leq \theta \leq 60°$ is determined from the combined CTE and CTC tests.

Herein, the combined concept of CTE and CTC tests for item (iii) is explained.

The points A and A' in Fig. 4 denote the present state of principal stress σ_{ij} and the subsequent state of principal stress $(\sigma_{ij} + d\sigma_{ij})$, respectively. The vector $\overrightarrow{AA'}$ or $d\sigma_{ij}$ is now projected onto the deviatoric stress plane (π-plane) as the vector $\overrightarrow{BB'}$, and onto the CTC-CTE plane as the vector $\overrightarrow{CC'}$. The vector $\overrightarrow{CC'}$ is on the intersecting line, which is the intersection between the CTC-CTE plane and the plane passing through the hydrostatic axis I_1 and the stress vector $\overrightarrow{AA'}$.

The deviatoric stress vector $\overrightarrow{BB'}$ on π-plane can now be further decomposed into two parts: $\overrightarrow{EE'}$ and $\overrightarrow{DD'}$ along the OE' and OD' axes respectively, as

$$dS_{ij} = dS^0_{ij} + dS^1_{ij} \tag{13}$$

where dS^0_{ij} and dS^1_{ij} are the components of the stress in the $\theta = 60°$ and $0°$ planes, respectively. From the geometry, the magnitudes of these components of dJ^1_2 on $0°$-plane and dJ^0_2 on $60°$-plane can be calculated from the total dJ_2 as

$$\left.\begin{aligned} dJ^0_2 &= dJ_2 \left[\cos(\pi/3-\theta) - \frac{1}{\sqrt{3}} \sin(\pi/3-\theta)\right]^2 \\ dJ^1_2 &= dJ_2 \left(\cos\theta - \frac{1}{\sqrt{3}} \sin\theta\right)^2 \end{aligned}\right\} \tag{14}$$

Since the deviatoric stresses dS^0_{ij} and dS^1_{ij} have the following characteristics:

$$\left.\begin{aligned} dS^0_{ij} &= (dS^0_{11},\ dS^0_{22},\ dS^0_{33}) = (dS^0_{11},\ -\tfrac{1}{2}\,dS^0_{11},\ -\tfrac{1}{2}\,dS^0_{11}) \\ dS^1_{ij} &= (dS^1_{11},\ dS^1_{22},\ dS^1_{33}) = (dS^1_{11},\ dS^1_{11},\ -2dS^1_{11}) \end{aligned}\right\} \tag{15}$$

Therefore, for the case of loading, the components of dS^0_{ij} and dS^1_{ij} can be calculated from Eqs. 14 and 15 as

$$\left.\begin{aligned} (dS^0_{11},\ dS^0_{22},\ dS^0_{33}) &= \left(-2\sqrt{\frac{dJ^0_2}{3}}\ ,\ \sqrt{\frac{dJ^0_2}{3}}\ ,\ \sqrt{\frac{dJ^0_2}{3}}\right) \\ \text{and} \qquad (dS^1_{11},\ dS^1_{22},\ dS^1_{33}) &= \left(-\sqrt{\frac{dJ^1_2}{3}}\ ,\ -\sqrt{\frac{dJ^1_2}{3}}\ ,\ 2\sqrt{\frac{dJ^1_2}{3}}\right) \end{aligned}\right\} \tag{16}$$

Similarly, the vector $\overrightarrow{CC'}$ with length dI_1 on the CTC-CTE plane can be decomposed as dI^0_1 and dI^1_1 onto the CTC line and CTE line respectively. From the geometry of Fig. 4, we have

$$\left.\begin{aligned} dI^0_1 &= dI_1\left[\frac{\cos(\pi/3-\theta) - \frac{1}{\sqrt{3}}\sin(\pi/3-\theta)}{2\cos\theta}\right] \\ dI^1_1 &= dI_1\left(1 - \frac{1}{\sqrt{3}}\tan\theta\right) \end{aligned}\right\} \tag{17}$$

Therefore, the decomposed principal stresses $d\sigma^0_{ij}$ and $d\sigma^1_{ij}$ can be rewritten as

$$
\left.
\begin{aligned}
d\sigma_{ij}^{0} &= \left(\frac{dI_1^0}{3} + dS_{11}^0,\ \frac{dI_1^0}{3} + dS_{22}^0,\ \frac{dI_1^0}{3} + dS_{33}^0\right) \\
d\sigma_{ij}^{1} &= \left(\frac{dI_1^1}{3} + dS_{11}^1,\ \frac{dI_1^1}{3} + dS_{22}^1,\ \frac{dI_1^1}{3} + dS_{33}^1\right)
\end{aligned}
\right\} \qquad (18)
$$

In the following, explicit expressions for calculating the strains are developed for the three proposed models: (1) nonlinear elasticity model with the Mohr-Coulomb or the Drucker-Prager failure surface; (2) cap model I; and (3) cap model II.

7. Incremental Constitutive Equations

7.1 Nonlinear Elasticity Model

In this modelling, behavior of materials is assumed to be elastic until the state of stress reaches the failure surface. For an isotropic, the bulk moduli K_0, K_1 and the shear moduli G_0, G_1 may be determined from the triaxial compression and triaxial tension tests. Two types of bulk moduli and shear moduli are considered.

(i) Bulk moduli and shear moduli are constant. This reduces to the linear elastic model.

(ii) Elastic bulk moduli K_0 and K_1 are assumed to be functions of the first invariant of the decomposed stress tensor I_1^0 and I_1^1, respectively,

$$
K_0 = K_0(I_1^0) \quad \text{and} \quad K_1 = K_1(I_1^1) \qquad (19)
$$

and elastic shear moduli G_0 and G_1 are assumed to be functions of the second invariant of the decomposed deviatoric stress tensor J_2^0 and J_2^1, respectively.

$$
G_0 = G_0\left(\sqrt{J_2^0}\right) \quad \text{and} \quad G_1 = G_1\left(\sqrt{J_2^1}\right) \qquad (20)
$$

According to the incremental Hooke's law, the strain increments $d\varepsilon_{ij}^0$ and $d\varepsilon_{ij}^1$ are written in terms of the decomposed stresses $d\sigma_{ij}^0$ and $d\sigma_{ij}^1$ as

$$\left.\begin{aligned} d\varepsilon^0_{ij} &= \frac{1}{9K_0}\, dI^0_1\, \delta_{ij} + \frac{1}{2G_0}\, dS^0_{ij} \\ d\varepsilon^1_{ij} &= \frac{1}{9K_1}\, dI^1_1\, \delta_{ij} + \frac{1}{2G_1}\, dS^1_{ij} \end{aligned}\right\} \qquad (21)$$

and the total strain increment $d\varepsilon_{ij}$ is the sum of the two components.

$$d\varepsilon_{ij} = d\varepsilon^0_{ij} + d\varepsilon^1_{ij} \qquad (22)$$

It should be noted that the direction of the total strain increment $d\varepsilon_{ij}$ is not necessary in the same direction as that of the total stress increment $d\sigma_{ij}$. The following shortcomings are noted in this modelling:

(i) The decomposition of dI_1 into two parts is not unique. Here, for convenience, we use the CTC-CTE planes.

(ii) The decomposition of dI_1 for the case of isotropic compression test can not be made because many combinations of decomposition can be considered.

(iii) For two stress paths which are extremely close to each other along the hydrostatic pressure axis but lie on two different planes $\theta = 0°$ and $60°$ respectively, the volumetric strains predicted with the corresponding bulk moduli K_0 and K_1 will have different values at the boundary of the hydrostatic axis.

The nonlinear elasticity model described above was used for predictions at the workshop.

7.2 Cap Model I

The conventional cap model used by Baladi [1], among others, has the Drucker-Prager type of yield surface with an elliptic cap. The size of the cap is assumed to have either a constant value or to be a function of the plastic volumetric strain. Since the Mohr-Coulomb failure surface is probably the best among all the failure criteria for soils, it follows that the size of the cap should depend not only on the plastic volumetric strain, but also on the Lode angle θ. In the present modelling, therefore,

two different caps are used. One is defined in the tensile meridian plane ($\theta = 0°$) and the other is defined in the compressive meridian plane ($\theta = 60°$). This is illustrated in Fig. 5-a, where the Mohr-Coulomb failure lines on these two planes are also shown.

In the elastic range, two types of bulk moduli K_0, K_1 and shear moduli G_0, G_1 may be considered.

(i) K_0, K_1, G_0 and G_1 are constants.

(ii) K_0, K_1 are functions of the first invariant of the decomposed stress tensor I_1^0 or I_1^1 and the plastic volumetric strains ε_{kk}^{P0} or ε_{kk}^{P1}, respectively,

$$\left.\begin{aligned} K_0 &= K_0\,(I_1^0,\ \varepsilon_{kk}^{P0}) \\ K_1 &= K_1\,(I_1^1,\ \varepsilon_{kk}^{P1}) \end{aligned}\right\} \tag{23}$$

and G_0, G_1 are functions of the second invariant of the decomposed stress tensor J_2^0 or J_2^1 and the plastic volumetric strains ε_{kk}^{P0} or ε_{kk}^{P1}.

$$\left.\begin{aligned} G_0 &= G_0\left(\sqrt{J_2^0},\ \varepsilon_{kk}^{P0}\right) \\ G_1 &= G_1\left(\sqrt{J_2^1},\ \varepsilon_{kk}^{P1}\right) \end{aligned}\right\} \tag{24}$$

where $d\varepsilon_{kk}^{P0}$ and $d\varepsilon_{kk}^{P1}$ are the plastic volumetric strains induced by the caps on $\theta = 60°$ and $0°$ planes, respectively.

The elastic strains $d\varepsilon_{ij}^{e}$ are calculated in the same manner as that used previously in the nonlinear elasticity model.

In the plastic range, the two elliptic caps located on the $\theta = 0°$ and $60°$ planes will contract or expand as the plastic volumetric strain ε_{kk}^{P} decreases or increases. The Mohr-Coulomb criterion is used here as the failure envelope which will not harden. The plastic strain $d\varepsilon_{ij}^{P}$ during the loading is derived from the flow rule (Eq. 12). The total plastic strain increment $d\varepsilon_{ij}^{P}$ is the sum of the plastic strain increments of $d\varepsilon_{ij}^{P0}$ and $d\varepsilon_{ij}^{P1}$ which are induced by the two caps:

$$d\varepsilon_{ij}^{P} = d\varepsilon_{ij}^{P0} + d\varepsilon_{ij}^{P1} \tag{25}$$

Each of the plastic strain increments can be written as

$$\left.\begin{aligned} d\varepsilon_{ij}^{P0} &= d\lambda^{0} \frac{\partial F_c^{0}}{\partial \sigma_{ij}^{0}} \\ d\varepsilon_{ij}^{P1} &= d\lambda^{1} \frac{\partial F_c^{1}}{\partial \sigma_{ij}^{1}} \end{aligned}\right\} \tag{26}$$

where $d\lambda^{0}$, $d\lambda^{1}$ are different positive scalar functions, F_c^{0}, F_c^{1} are the elliptic cap functions and σ_{ij}^{0}, σ_{ij}^{1} are the decomposed stresses, respectively. From Eqs. 25 and 26, we have

$$\left.\begin{aligned} d\varepsilon_{ij}^{P0} &= d\lambda^{0}\left[\frac{\partial F_c^{0}}{\partial I_1^{0}} \frac{\partial I_1^{0}}{\partial \sigma_{ij}^{0}} + \frac{\partial F_c^{0}}{\partial \sqrt{J_2^{0}}} \frac{\partial \sqrt{J_2^{0}}}{\partial J_2^{0}} \frac{\partial J_2^{0}}{\partial \sigma_{ij}^{0}}\right] \\ d\varepsilon_{ij}^{P1} &= d\lambda^{1}\left[\frac{\partial F_c^{1}}{\partial I_1^{1}} \frac{\partial I_1^{1}}{\partial \sigma_{ij}^{1}} + \frac{\partial F_c^{1}}{\partial \sqrt{J_2^{1}}} \frac{\partial \sqrt{J_2^{1}}}{\partial J_2^{1}} \frac{\partial J_2^{1}}{\partial \sigma_{ij}^{1}}\right] \end{aligned}\right\} \tag{27}$$

The total strain increment $d\varepsilon_{ij}$ is the sum of the elastic strain and plastic strain increments.

$$d\varepsilon_{ij} = \left[\frac{dI_1^{0}}{9K_0(I_1^{0},\ \varepsilon_{kk}^{P0})} + \frac{dI_1^{1}}{9K_1(I_1^{1},\ \varepsilon_{kk}^{P1})}\right]\delta_{ij} +$$

$$\left[\frac{dS_{ij}^{0}}{2G_0\left(\sqrt{J_2^{0}},\ \varepsilon_{kk}^{P0}\right)} + \frac{dS_{ij}^{1}}{2G_1\left(\sqrt{J_2^{1}},\ \varepsilon_{kk}^{P1}\right)}\right] +$$

$$d\lambda^0 \left[\frac{\partial F_c^0}{\partial I_1^0} \delta_{ij} + \frac{1}{2\sqrt{J_2^0}} \frac{\partial F_c^0}{\partial \sqrt{J_2^0}} S_{ij}^0 \right] +$$

$$d\lambda^1 \left[\frac{\partial F_c^1}{\partial I_1^1} \delta_{ij} + \frac{1}{2\sqrt{J_2^1}} \frac{\partial F_c^1}{\partial \sqrt{J_2^1}} S_{ij}^1 \right] \tag{28}$$

Eq. 28 is the incremental stress-strain relations corresponding to the proposed cap model I. In order to use this relation (Eq. 28) for a stress analysis, the scalar functions $d\lambda^0$ and $d\lambda^1$ must be determined. Using the consistency condition $dF_c = 0$ during loading and Eq. 12, $d\lambda^0$, $d\lambda^1$ can be derived in a straightforward manner as

$$d\lambda^0 = \frac{3K_0 \frac{\partial F_c^0}{\partial I_1^0} d\varepsilon_{kk}^0 + \frac{G_0}{\sqrt{J_2^0}} \frac{\partial F_c^0}{\partial \sqrt{J_2^0}} S_{ij}^0 de_{ij}^0}{9K_0 \left[\frac{\partial F_c^0}{\partial I_1^0}\right]^2 + G_0 \left[\frac{\partial F_c^0}{\partial \sqrt{J_2^0}}\right]^2 - 3 \frac{\partial F_c^0}{\partial I_1^0} \frac{\partial F_c^0}{\partial \varepsilon_{kk}^{P0}}} \tag{29}$$

where de_{ij}^0 is the strain corresponding to the decomposed deviatoric stress dS_{ij}^0. Also, $d\lambda^1$ has the same form as that of Eq. 29 except changing the subscript from 0 to 1. For the states of stresses on the Mohr-Coulomb surface, the corresponding plastic strain increment $d\varepsilon_{ij}^P$ is derived from the flow rule:

$$d\varepsilon_{ij}^P = d\lambda \frac{\partial F_L}{\partial \sigma_{ij}} \tag{30}$$

where F_L is the Mohr-Coulomb failure function, σ_{ij} is the total stress and $d\lambda$ is a positive scalar function.

The main characteristics of this model are:

(i) The direction of the strain increment $d\varepsilon_{ij}$ is not necessary in the same direction as that of the stress increment $d\sigma_{ij}$ even with elastic region.

(ii) The hardening caps exist only in the $\theta = 0°$ and $\theta = 60°$ planes. Two caps control the hardening of the isotropic materials within the range of 0° to 60°.

The limitations of this model are:

(i) The same limitations as that of nonlinear elasticity model described previously.

(ii) Because this model assumes two independent caps, the model may predict a total plastic volumetric strain ε^P_{kk} that may exceed the maximum plastic strain W.

(iii) The intersections of the caps with I_1-axis are not the same. The model does not satisfy the continuity condition along the hydrostatic axis.

7.3 Cap Model II

This model can be considered as a generalization of the cap model I described in the preceding section. The two caps in the $\theta = 0°$ and 60° planes are now connected by a three-dimensional cap as shown in Fig. 5-b.

In the elastic range, the same procedure as that of Cap Model I is used for the elastic strain calculation. However, the bulk modulus K_0 or K_1 is now a function of I_1^0 or I_1^1 and the total plastic volumetric strain ε^P_{kk}, while the shear modulus G_0 or G_1 is a function of $\sqrt{J_2^0}$ or $\sqrt{J_2^1}$ and the total plastic volumetric strain ε^P_{kk}, respectively. Similarly, the plastic strain increment is determined from Eq. 12. Thus, the total strain increment $d\varepsilon_{ij}$ is written as

$$d\varepsilon_{ij} = \left[\frac{dI_1^0}{9K_0(I_1^0, \varepsilon^P_{kk})} + \frac{dI_1^1}{9K_1(I_1^1, \varepsilon^P_{kk})}\right]\delta_{ij} + \left[\frac{dS_{ij}^0}{2G_0\left(\sqrt{J_2^0}, \varepsilon^P_{kk}\right)}\right.$$

$$+ \frac{dS_{ij}^{1}}{2G_1\left(\sqrt{J_2^1}, \varepsilon_{kk}^{P}\right)}\Bigg] + d\lambda\left[\frac{\partial F_c}{\partial I_1}\delta_{ij} + \frac{1}{2\sqrt{J_2}}\frac{\partial F_c}{\partial \sqrt{J_2}}S_{ij}\right] \tag{31}$$

where $d\lambda$ is derived using the same procedure as in Cap Model I.

For the stress state on the Mohr-Coulomb failure surface, the plastic strain increment is given by Eq. 30.

8. Model Calibration

General

In the workshop, three sets of soil materials are available for prediction under different stress paths. These are "Clay X", "Clay Y", "Kaolinite Clay" and "Ottawa Sand". Herein, nonlinear elasticity model is applied to predict the behavior of all three materials. Further, plasticity models (Cap Model I and Cap Model II) are applied only to "Clay X" and "Clay Y".

In the following, the stress paths used in the experiments and in the predictions are first defined. Then, the general procedure for determining the material constants for the three models is explained, and the stress-strain relations corresponding to particular stress paths are derived. Herein, typical soil mechanics sign convention (compressive stress positive) is used in the model calibration.

8.1 Stress Paths in Experiments

The stress path used in the experiments can be described by the stress ratio m.

$$m = \frac{\sigma_2 - \sigma_3}{\sigma_1 - \sigma_3} \tag{32}$$

where σ_1, σ_2 and σ_3 are the principal stresses applied to the cylindrical or the cubic soil spedimen and σ_1 is the stress in the vertical or axial direction.

The stress path with the ratio $m = 0$ or $m = 1$ is on the plane $\theta = 60°$ or $\theta = 0°$ respectively. The stress path corresponding to a simple shear test as viewed in the π-plane is shown in Fig. 6-a. If the Lode angle θ is defined from the plane, $m = 0$, then, the relation between θ and m is given by

$$\cos\theta = \frac{(2-m)(1-2m)(1+m)}{2(m^2-m+1)^{3/2}} \tag{33}$$

The stress path corresponding to conventional triaxial test lies between the stress path CTC test and the path CTE test as shown in Fig. 6-b in $I_1 - \sqrt{J_2}$ space.

8.2 Determination of Material Constants and Analysis

General

For the nonlinear elasticity model, we need to determine the bulk moduli K_0 and K_1, shear moduli G_0 and G_1. The bulk modulus K is a function of I_1 and is determined by an isotropic compression test. The shear moduli G_0 and G_1 are functions of $\sqrt{J_2^0}$ and $\sqrt{J_2^1}$ and are determined by the stress difference-strain difference curves from drained triaxial compression and tension tests conducted at different levels of confining pressure. If the model is applied to problems involved cyclic and reversed loading, bulk modulus K, and the shear moduli G_0 and G_1 can be determined respectively by the unloading curves of the tests mentioned above. Hence, the variable moduli model is used.

For the plasticity models, the bulk modulus K and the shear moduli G_0 and G_1 can be determined from the slopes of the unloading curves of an isotropic compression test; and from the slopes of the unloading stress difference-strain difference curves of a drained triaxial compression tests and tension tests at different levels of confining pressure, respectively. In the plastic range, the values of α and k are obtained from c and ϕ values associated with the Mohr-Coulomb failure envelope, which is constructed through simple shear tests. The material constants W and D in Eq. 10 associated with the hardening function are determined by isotropic compression and unloading tests. The constant R associated with cap shape is determined from simple shear and uniaxial strain tests. The choice

of material constants R from experimental data requires a considerable experience.

Clay X

The experimental data on the simple shear tests with the stress ratio $m = 0$ and 1 under confining pressure σ_c = 10, 20 and 30 psi are available. The nonlinear elasticity model, cap model I and cap model II are used for prediction. In the case of nonlinear elasticity model, the stress difference-strain difference curves are drawn for each confining pressure as shown in Figs. 7 through 9 where we have used the average values of ε_1 and ε_2, or ε_2 and ε_3. These curves are fitted by a function using nonlinear regression analysis. In general, the relation between stress difference and strain difference can be expressed as

$$\sigma_1 - \sigma_3 = f(\varepsilon_1^* - \varepsilon_3 \text{ or } \varepsilon_1 - \varepsilon_3^*) \tag{34}$$

Taking derivative with respect to the strain difference, we have

$$\left.\begin{aligned} G_0 \text{ or } G_1 &= g(\sigma_1^0 - \sigma_3^0 \text{ or } \sigma_1^1 - \sigma_3^1) \\ \text{or} \\ G_0 \text{ or } G_1 &= g(\sqrt{3J_2^0} \text{ or } \sqrt{3J_2^1}) \end{aligned}\right\} \tag{35}$$

Each pair of G_0 and G_1 functions are utilized for the present prediction under different confining pressure. The matchings of the Mohr-Coulomb constants (c, ϕ) and the Drucker-Prager constants (α, k) are listed in Table 1 for all three materials. The principal stress increments $d\sigma_{11}$, $d\sigma_{22}$ and $d\sigma_{33}$ can be written in the form as

$$\left.\begin{aligned} d\sigma_{11} &= d\sigma_{11} \\ d\sigma_{22} &= \frac{2m-1}{2-m}\, d\sigma_{11} \\ d\sigma_{33} &= \frac{m+1}{m-2}\, d\sigma_{11} \end{aligned}\right\} \tag{36}$$

from which dJ_2 can be expressed in terms of $d\sigma_{11}$. Thus, for a given $d\sigma_{11}$, the corresponding strain increment $d\varepsilon_{ij}$ can be computed. The process continues until the stress path reaches the Mohr-Coulomb or Drucker-Prager failure surface.

In the case of plasticity models, clay X is assumed to be an anisotropic material. Fig. 10 shows the relation between the stress increment $d\sigma^0_{11}$ or $d\sigma^1_{11}$ and each strain increment.

The stress-strain relation can be regarded as linear up to $d\sigma^0_{11}$ of 5 psi or $d\sigma^1_{11}$ of 2 psi, respectively. Thus, the following relation is assumed in the leastic range, for $m = 0$

$$d\varepsilon^0_{11} = 0.0014\ d\sigma^0_{11},\ d\varepsilon^0_{22} = -0.00156\ d\sigma^0_{11} \text{ and } d\varepsilon^0_{33} = 0.0002\ d\sigma^0_{11} \tag{37}$$

and for $m = 1$,

$$d\varepsilon^1_{11} = 0.00325\ d\sigma^1_{11},\ d\varepsilon^1_{22} = -0.00267\ d\sigma^1_{11} \text{ and } d\varepsilon^1_{33} = -0.00055\ d\sigma^1_{11} \tag{38}$$

The constants W and D are estimated to be 0.3174 and 0.0087, respectively. Therefore, Eq. 10 is

$$\varepsilon^P_{kk} = 0.3174\ [1 - e^{-0.0087(x-46.5)}] \tag{39}$$

where the value 46.5 is three times of the preconsolidation pressure σ_p (compressive stress taken as positive). The material constants R (cap shape) are determined to be 4.7 from the simple shear test data with the stress ratio $m = 0$ and to be 5.7 from those with the stress ratio $m = 1$. Fig. 11 shows the location of hardening caps for the planes of $m = 0$ and $m = 1$ in $I_1 - \sqrt{J_2}$ space. The plastic strain increments $d\varepsilon^P_{ij}$ are calculated for the cases of Cap Model I and Cap Model II. As the experiments have been conducted under stress control condition, the plastic volumetric strain increment $d\varepsilon^P_{kk}$ can be calculated from Eq. 39 after the value of x is obtained from the subsequent state of stress and elliptic cap equation. Therefore, $d\lambda$ is obtained from Eq. 12.

For cap model I,

$$d\lambda^0 = \frac{d\varepsilon_{kk}^{P0}}{\frac{\partial F_c^0}{\partial \sigma_{ij}^0}} \quad \text{and} \quad d\lambda^1 = \frac{d\varepsilon_{kk}^{P1}}{\frac{\partial F_c^1}{\partial \sigma_{ij}^1}} \tag{40}$$

and for cap model II,

$$d\lambda = \frac{d\varepsilon_{kk}^{P}}{\frac{\partial F_c}{\partial \sigma_{ij}}} \tag{41}$$

Therefore, the plastic strain increment $d\varepsilon_{ij}^P$ is obtained from Eq. 12 respectively.

Clay Y

The experimental data are obtained from the triaxial tests with the stress ratio m = 0 and m = 1 under the initial confining pressure σ_c = 2.5, 5.0 and 10 psi. The property of clay Y appears to be similar to that of clay X. As the initial location of confining pressure lies on "Dry of Critical" from viewpoint of the critical state soil mechanics, the Coulomb constants c and ϕ (in Table 1) are different from those constants for clay X. The experimental data indicate that the behavior of clay Y appears to be isotropic. Therefore, the stress difference-strain difference relation, and the stress invariant I_1 - the volumetric strain relation are checked for three sets of data as shown in Fig. 12 through 14. For nonlinear elasticity model, the functions of bulk moduli K_0, K_1 and shear moduli G_0, G_1 are obtained using the curve fitting procedure similar to that of clay X. The principal stress increments $d\sigma_{11}$, $d\sigma_{22}$ and $d\sigma_{33}$ with the stress ratio m is expressed in terms of $d\sigma_{11}$ by

$$d\sigma_{11} = d\sigma_{11}, \quad d\sigma_{22} = m\,d\sigma_{11} \text{ and } \quad d\sigma_{33} = 0 \tag{42}$$

The corresponding strain increment can be calculated as that of clay X.

For the plasticity models, the stress-strain relations are again checked for the data with m = 0 and 1 as shown in Fig. 15. The shear modulus G_0 for m = 0 or G_1 for m = 1 is assumed to be a function of $\sqrt{J_2^0}$ or constant, respectively. The bulk moduli K_0 and K_1 are assumed to be two different constants respectively. The material constants W and D are estimated to be 0.135 and 0.009. Therefore, Eq. 10 is

$$\varepsilon_{kk}^{P} = 0.135\ [1 - e^{-0.009(x-46.5)}] \tag{43}$$

where the preconsolidation pressure σ_p is assumed to be the same as that in clay X.

The material constants R (cap shape) are determined to be 2.39 from the triaxial test data with m = 0 and to be 0.87 from those with m = 1. The location of hardening caps are shown in Fig. 16. The calculation of the strain increment is the same as that of clay X.

Kaolinite Clay

The available experimental data are the triaxial tests (No. 1 and 10) and the simple shear tests (No. 4 and 13) with m = 0 or m = 1 under an undrained condition. The nonlinear elasticity model is utilized for the prediction.

The experimental data are plotted in the stress difference-the strain difference space as shown in Fig. 17. Here, as in the previous case, the stress difference-the strain difference curves are fitted by functions in order to determine the shear moduli G_0 and G_1 which are functions of J_2. For these tests to be predicted by the model, the major principal stress is inclined at an angle to the vertical axis of the specimen, while the intermediate principal stress remains horizontal. Since the material is assumed to be isotropic for present case, the direction of the applied principal stresses will not affect the results of prediction. The increments of principal stresses with stress ratio m are expressed in terms of $d\sigma_{11}$ by

$$d\sigma_{11} = d\sigma_{11}, \quad d\sigma_{22} = 0 \quad \text{and} \quad d\sigma_{33} = \frac{m}{m-1}\, d\sigma_{11} \tag{44}$$

for Test No. 2, 3, 7, 11 and 12 and

$$d\sigma_{11} = d\sigma_{11},\ d\sigma_{22} = \frac{1-2m}{m-2}\, d\sigma_{11} \text{ and } d\sigma_{33} = \frac{m+1}{m-2}\, d\sigma_{11} \tag{45}$$

for Test No. 5, 6, 8 and 9.

It should be noted that those principal stresses are the total principal stresses because the tests are conducted under an undrained condition. Therefore, the effective principal stress increments must be known in order to calculate the principal strain increments. In this case, the effective stress increments are the deviatoric stress increments dS_{ij} because the inclusion of hydrostatic pressure increment dI_1 causes a volumetric change. Thus, the effective stress increments are calculated from Eqs. 44 and 45, and the corresponding strain increments can be calculated in a same manner as that described above.

Ottawa Sand

The experimental data available for predictions are the conventional triaxial compression tests under the initial confining pressure of 5, 10 psi, the conventional triaxial tension test under the initial confining pressure of 5 psi, and the simple shear tests with the stress ratio of $m = 0$, 1 under the mean normal stresses of 5, 10 and 20 psi.

Here, as the experimental data for the loading, unloading and reloading cases are given, the variable moduli model is used. In order to determine the shear moduli G_0 and G_1 for the loading case, the experimental data for the loading parts in the simple shear tests are plotted in the space of the strain difference and the stress difference divided by the stress difference at each failure (Fig. 18). The curves used in the prediction are shown by the dotted curves which are obtained by a nonlinear regression analysis. Thus, the shear moduli G_0^L and G_1^L for the loading cases are given by

$$\left.\begin{aligned} G_0^L &= G_0^L\left(\sigma_f^0, \sqrt{J_2^0}\right) \\ \text{and} \qquad G_1^L &= G_1^L\left(\sigma_f^1, \sqrt{J_2^1}\right) \end{aligned}\right\} \tag{46}$$

where σ_f^0 and σ_f^1 are the stress differences at failure in CTC and CTE tests. The stress difference at a failure is given by

$$\sigma_f^0 = \frac{6(c\cos\phi + \sigma_m \sin\phi)}{3 - \sin\phi} \tag{47-a}$$

for the modulus G_0^L and

$$\sigma_f^1 = \frac{6(c\cos\phi + \sigma_m \sin\phi)}{3 + \sin\phi} \tag{47-b}$$

for the modulus G_1^L, where σ_m is the mean normal stress. In this case, the shear moduli are functions of I_1 and J_2^0 or J_2^1.

To determine the shear moduli G_0^{ur}, G_1^{ur} for the unloading and reloading cases, the experimental data for the unloading and reloading parts in the simple shear tests are plotted in Fig. 19. In this case, the stress difference and the strain difference are measured from the unloading and reloading points. The curves used in the prediction are shown by the dotted curves. Thus, the shear moduli G_0^{ur} and G_1^{ur} have the same form as that in Eq. 46.

The bulk modulus K_0 and K_1 are determined from the conventional triaxial compression and tension tests. Although the data on the isotropic consolidation test are given, they are not used here to determine the bulk moduli. The experimental data are plotted in I_1 and ε_{kk} space as shown in Fig. 20. The bulk moduli K_0^L and K_1^L for the loading up to the unloading point, K_0^{ur} and K_1^{ur} for the unloading, reloading up to the point of previous unloading, and K_0^{NL} and K_1^{NL} for the loading starting from the point of the previous unloading are determined from the figure. These bulk moduli appear to depend on the initial confining pressure σ_c. Therefore, the general form for K may be written as

$$K = K(\sigma_c) \tag{48}$$

In general, the bulk modulus of Ottawa sand may be expressed by $K = K(\sigma_{max})$ where σ_{max} is a maximum confining pressure similar to the preconsolidation pressure.

The calculation of the strain can be carried out in the same way as mentioned previously.

9. Acknolwedgments

This material is based upon work supported by the National Science Foundation under Grant No. PFR-7809326 to Purdue University.

References

[1] Baldi, G. Y. and Rohani, B., "An Elastic-Plastic Constitutive Model for Saturated Sand Subjected to Monotonic and/or Cyclic Loadings," Third International Conference on Numerical Method in Geomechanics, Aachen, 2-6 April 1979, pp. 389-404.

[2] Chen, W. F., "Limit Analysis and Soil Plasticity," Elsevier, Amsterdam, The Netherlands, 1975.

[3] Chen, W. F., "Plasticity in Soil Mechanics and Landslides," Engineering Mechanics Division, ASCE, Vol. 106, No. EM3, June, 1980, pp. 443-464.

[4] Chen, W. F. and Mizuno, E., "On Material Constants for Soil and Concrete Models," Third ASCE/EMD Specialty Conference, 1979, pp. 539-542.

[5] DiMaggio, F. L. and Sandler, I. S., "Material Models for Granular Soils," Journal of the Engineering Mechanics Division, ASCE, Vol. 97, No. EM3, 1971, pp. 936-950.

[6] Drucker, D. C., Gibson, R. E., and Henkel, D. J., "Soil Mechanics and Work-Hardening Theories of Plasticity," Transactions, ASCE, Vol. 122, 1957, pp. 338-346.

[7] Drucker, D. C. and Prager, W., "Soil Mechanics and Plastic Analysis or Limit Design," Quarterly of Applied Mathematics, Vol. 10, No. 2, July 1952, pp. 157-175.

[8] Mizuno, E. and Chen, W. F., "Analysis of Soil Response with Different Plasticity Models," ASCE Symposium in Florida, 1980.

[9] Roscoe, K. H., Schofield, A. N., and Thurairajah, A., "Yielding of Clays in State Wetter than Critical," Géotechnique, Vol. 13, No. 3, 1963, pp. 211-240.

[10] Sandler, I. S., DiMaggio, F. L., and Baladi, G. Y., "Generalized Cap Model for Geological Materials," Geotechnical Division, ASCE, Vol. 102, No. GT. 7, 1976, pp. 683-699.

[11] Sandler, I. S. and Melvin, L. B., "Material Models of Geological Materials in Ground Shock," Numerical Method in Geomechanics. Edited by C. S. Desai, Vol. 1, 1976, pp. 219-231.

[12] Schofield, A. N. and Wroth, P., "Critical State Soil Mechanics," McGraw-Hill, New York, 1968.

[13] Zienkiewicz, O. C., "The Finite Element Method," McGraw-Hill, 1978 (Chap. 18).

[14] Zienkiewicz, O. C., Humpheson, C., and Lewis, R. W., "Associated and Non-Associated Visco-Plasticity and Plasticity in Soil Mechanics," Géotechnique, 25, No. 4, 1975, pp. 671-689.

Table 1 Material Constants c, ϕ, α and k

Material Constants	Clay X	Clay Y	Kaolinite Clay	Ottawa Sand
C (psi)	2.0	4.0	13.75	2.0
ϕ (°)	26.57	16.88	17.04	42.34
$\frac{2 \sin \phi}{\sqrt{3}(3-\sin \phi)}$	0.2023	0.1221	0.1250	0.2117
$\frac{6c \cos \phi}{\sqrt{3}(3-\sin \phi)}$	2.4275	4.892	16.823	1.394
$\frac{2 \sin \phi}{\sqrt{3}(3+\sin \phi)}$	0.1498	0.10	0.1027	0.334
$\frac{6c \cos \phi}{\sqrt{3}(3+\sin \phi)}$	1.7976	4.304	13.830	2.201

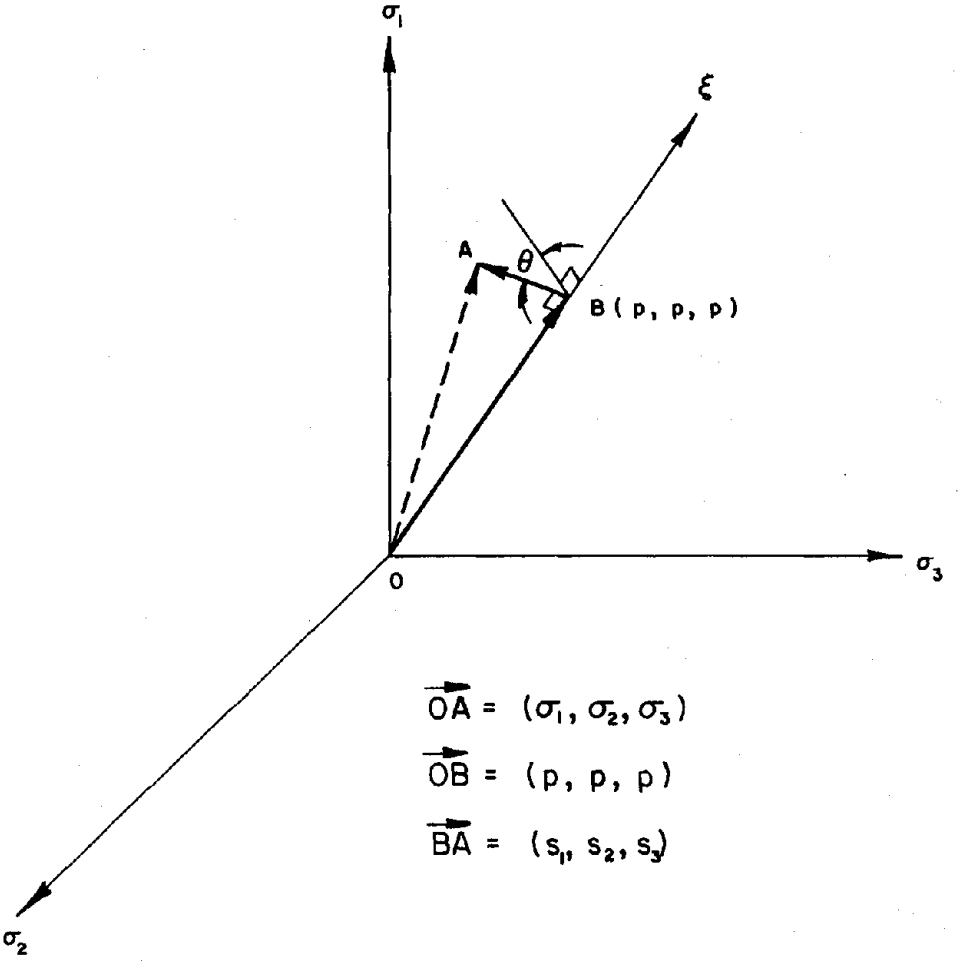

Fig. 1 Stress State in Principal Stress Space

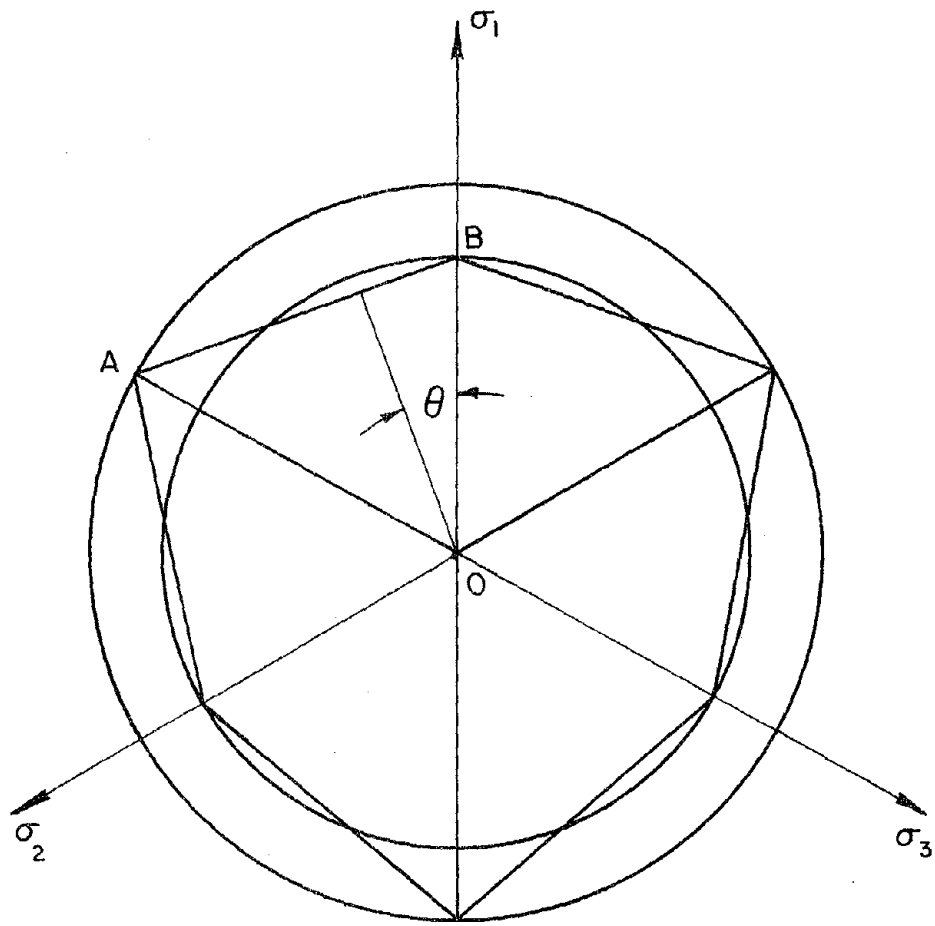

Fig. 2 Shape of Yield Criterion on π-Plane

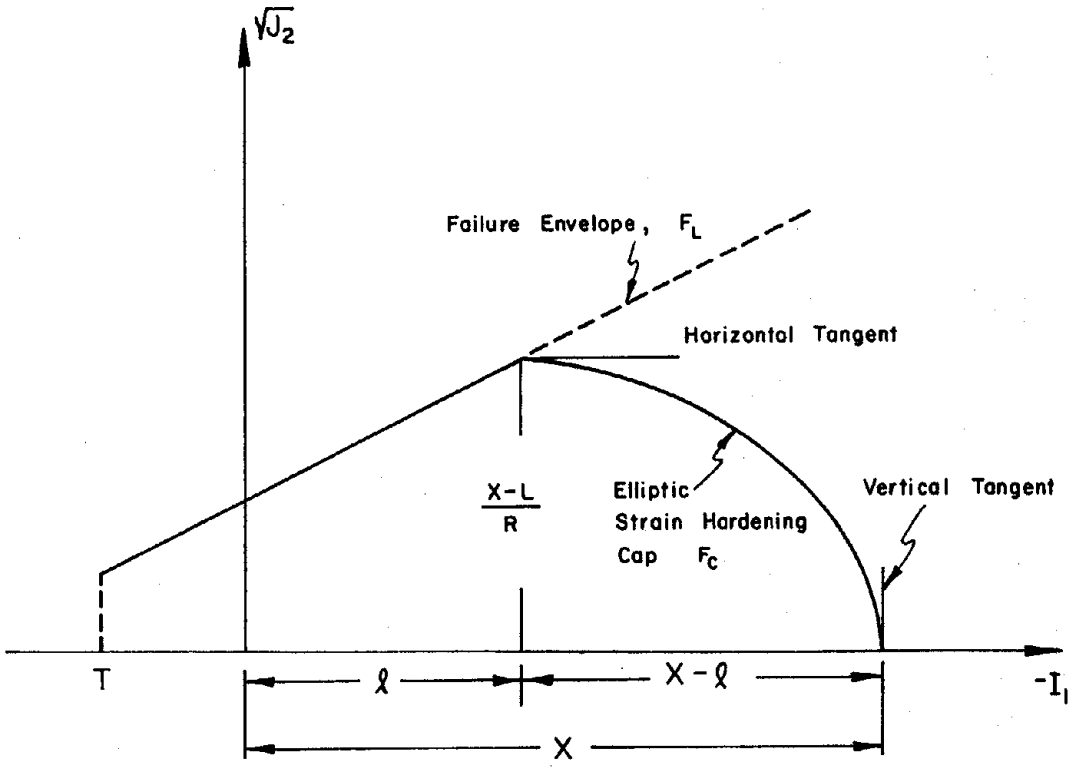

Fig. 3 Elliptic Cap Model

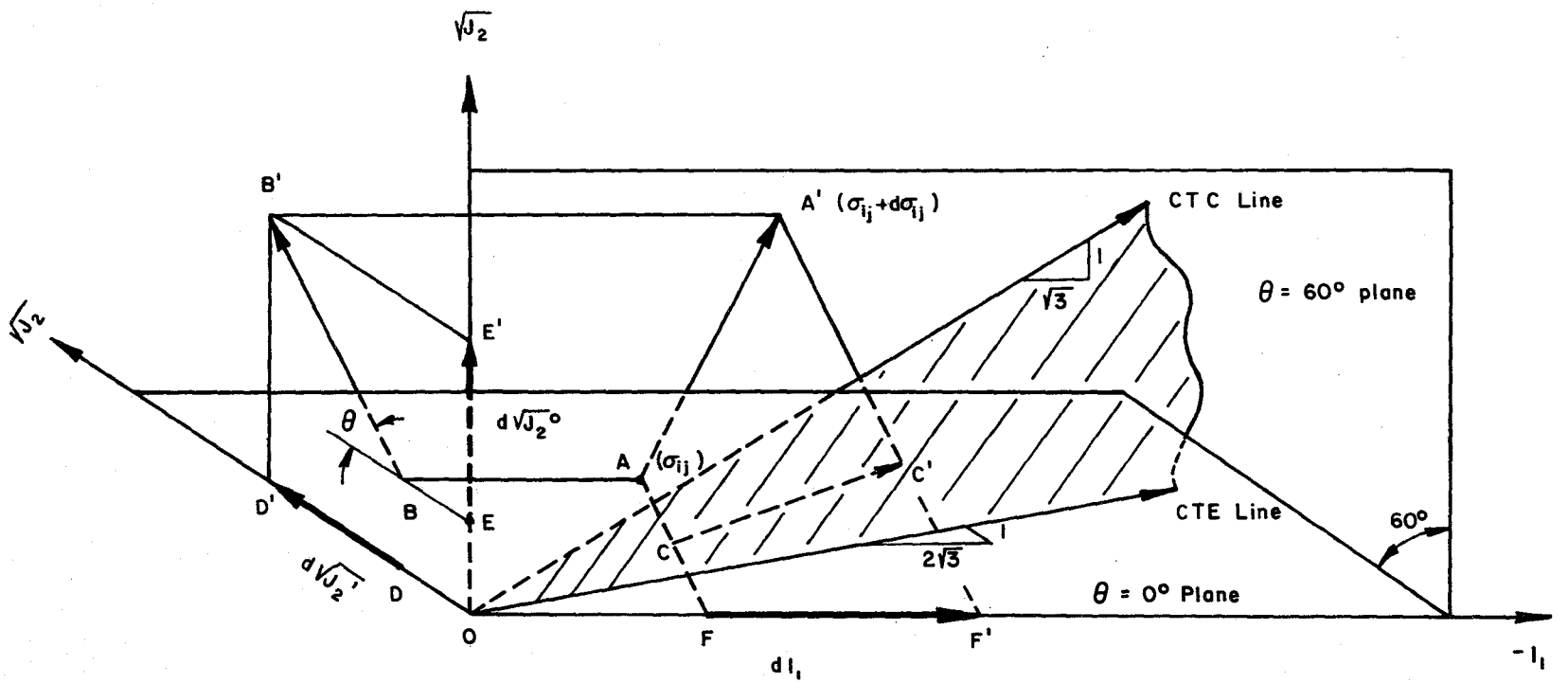

Fig. 4 General Stress Path in $I_1 - \sqrt{J_2}$ Space

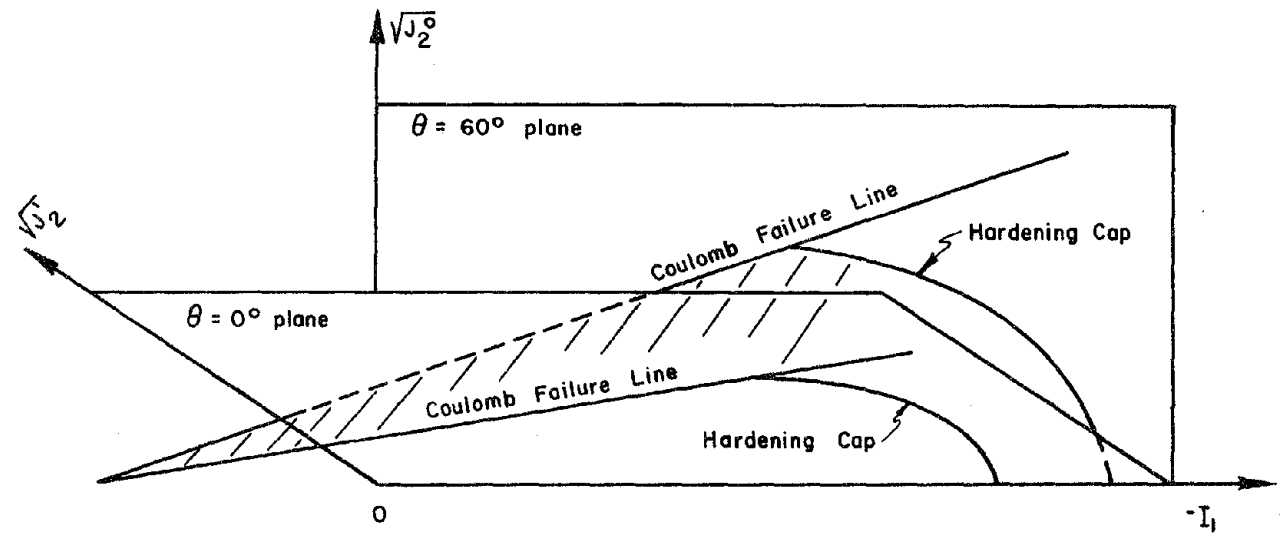

a) Cap Model I

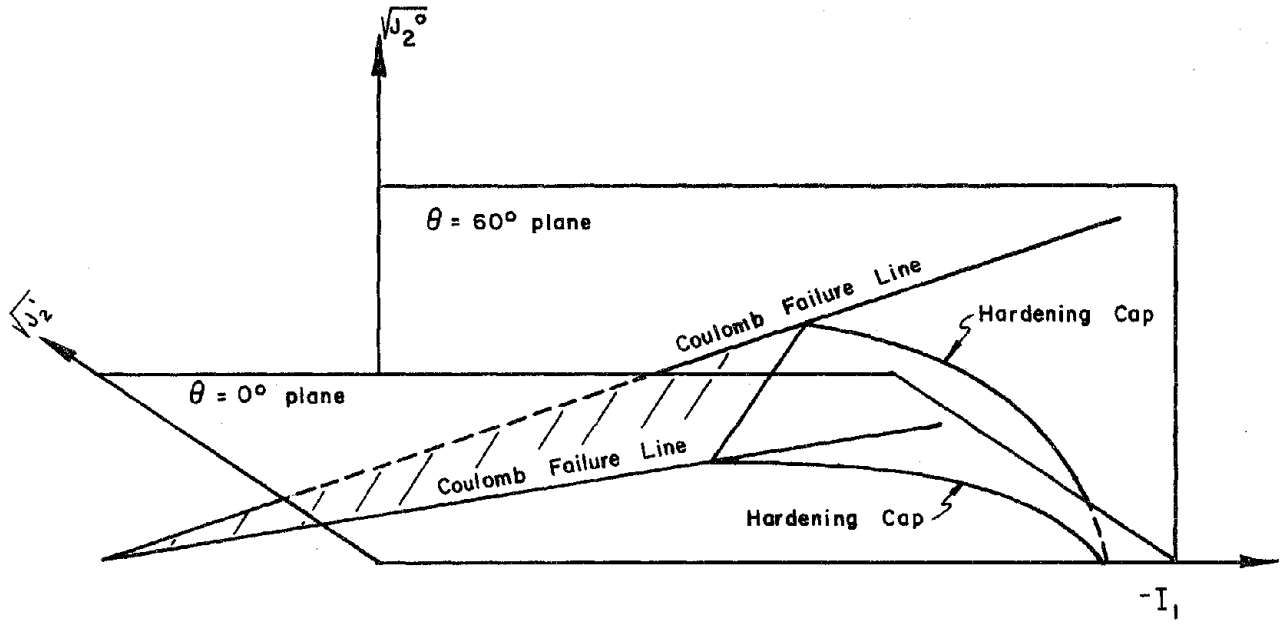

b) Cap Model II

Fig. 5 Scheme of Cap Model I and Cap Model II

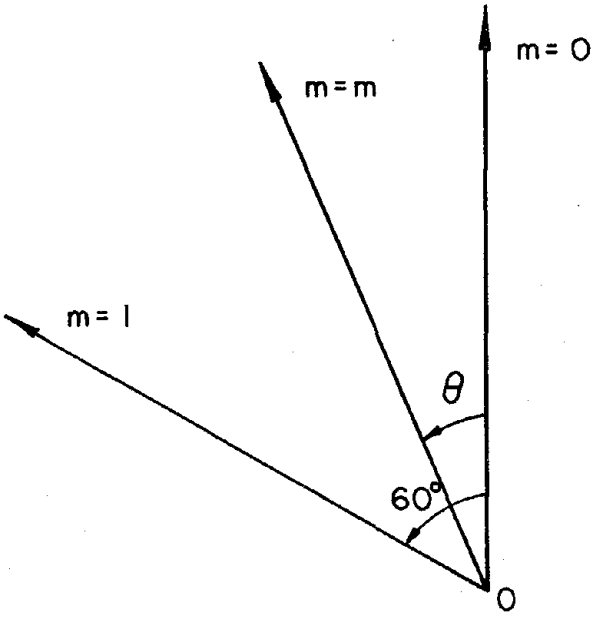

a) Stress Path on π - Plane

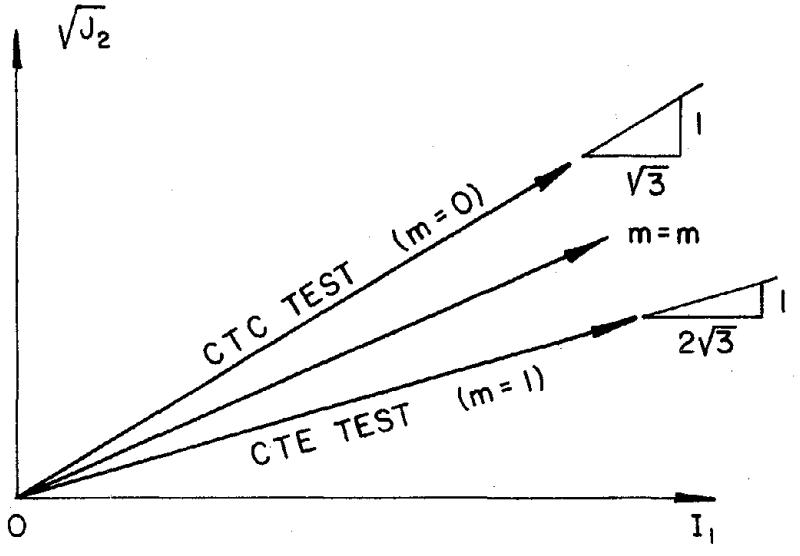

b) Stress Path in I_1-$\sqrt{J_2}$ Space

Fig. 6 Stress Path in Experiments

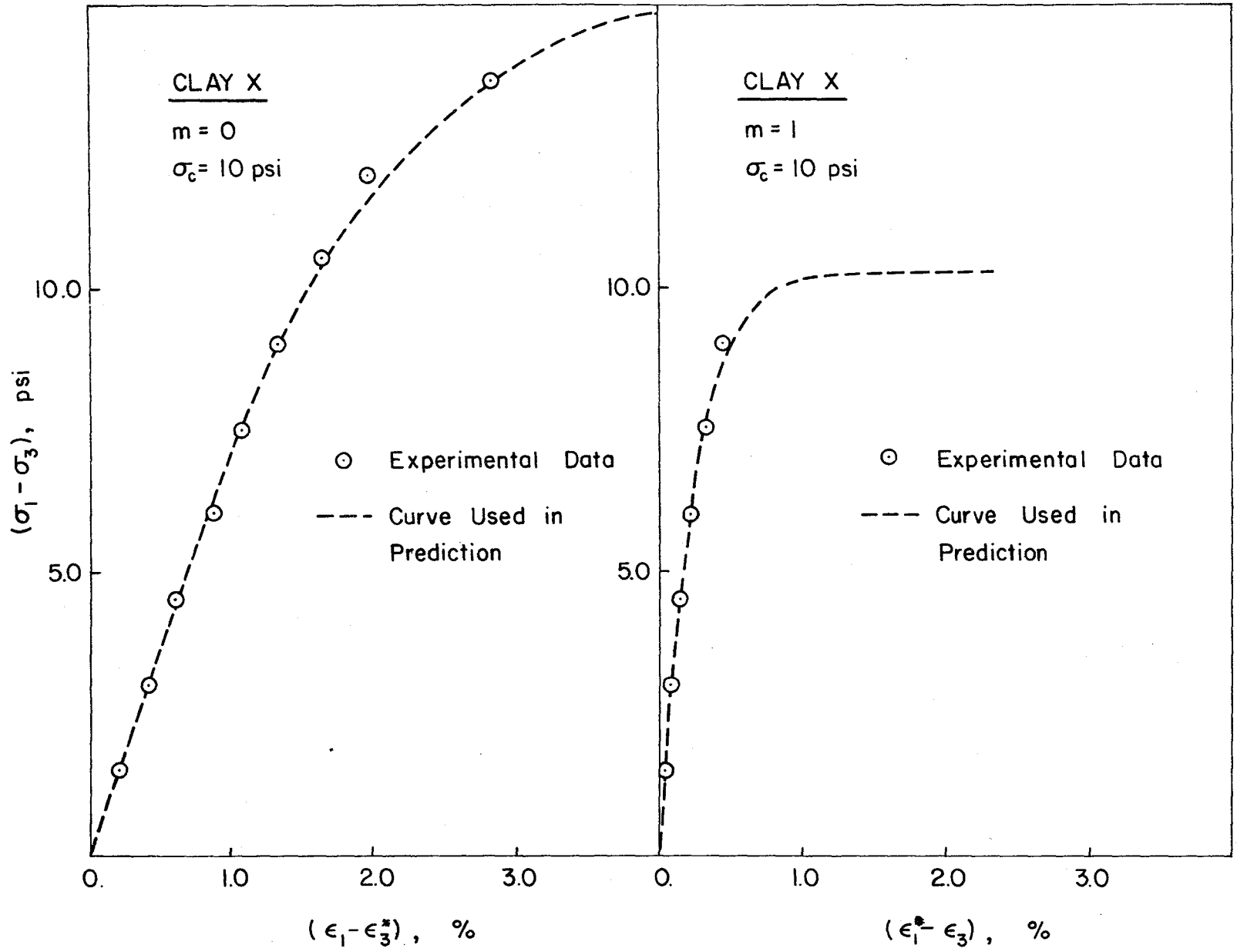

Fig. 7 Calibration of Shear Moduli for Clay X (σ_c = 10 psi, Nonlinear Elasticity Model)

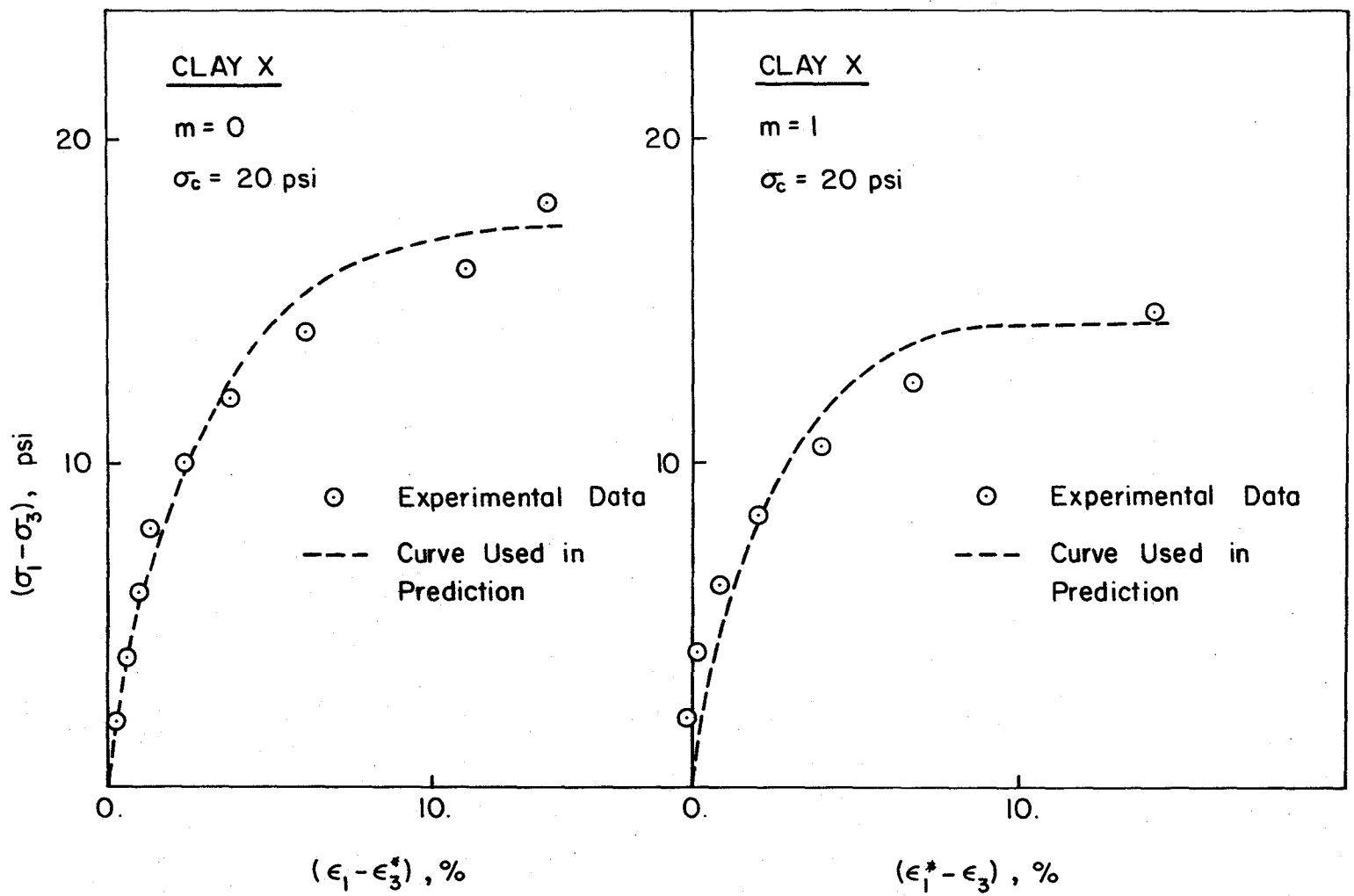

Fig. 8 Calibration of Shear Moduli for Clay X (σ_c = 20 psi, Nonlinear Elasticity Model)

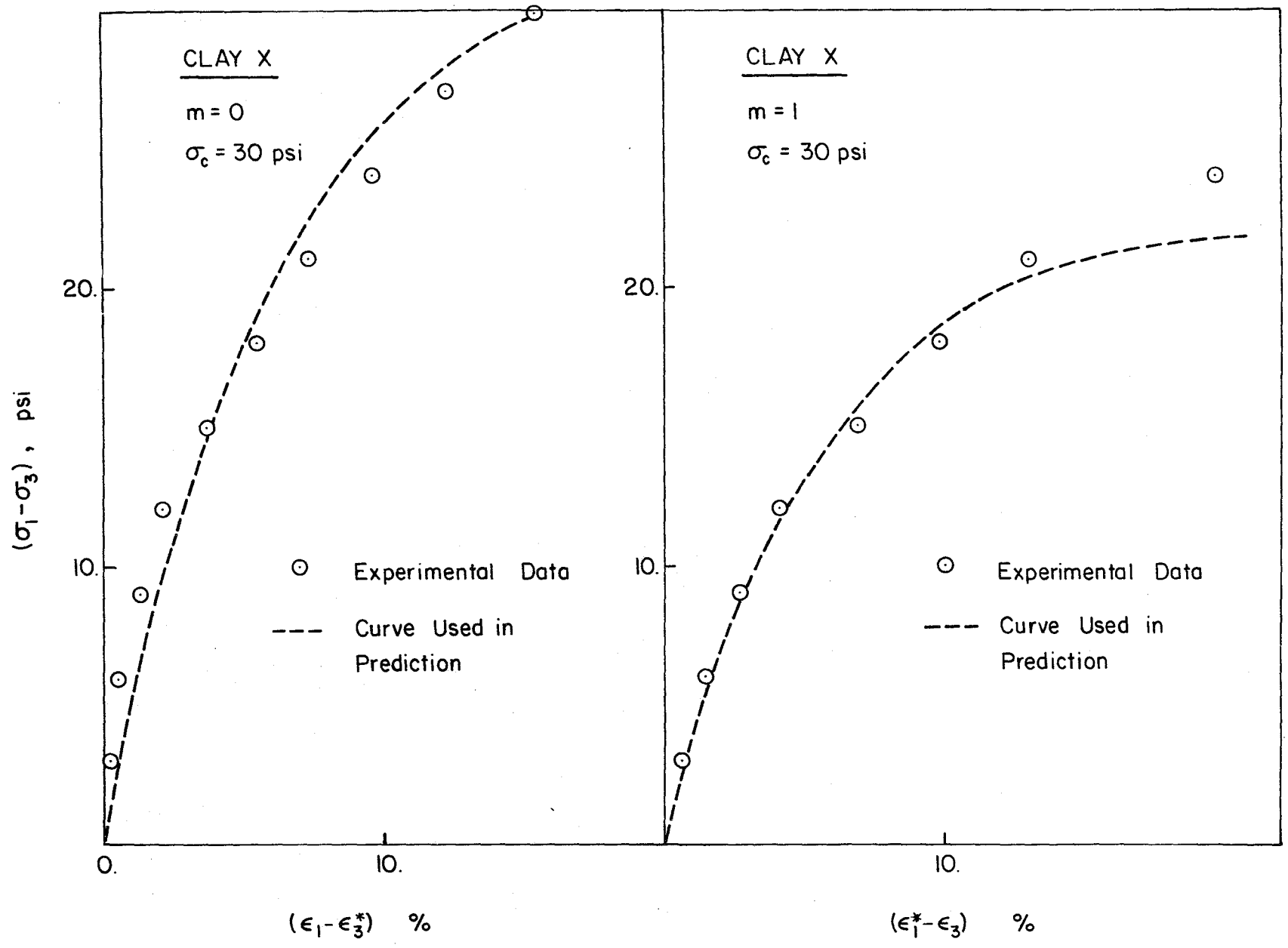

Fig. 9 Calibration of Shear Moduli for Clay X (σ_c = 30 psi, Nonlinear Elasticity Model)

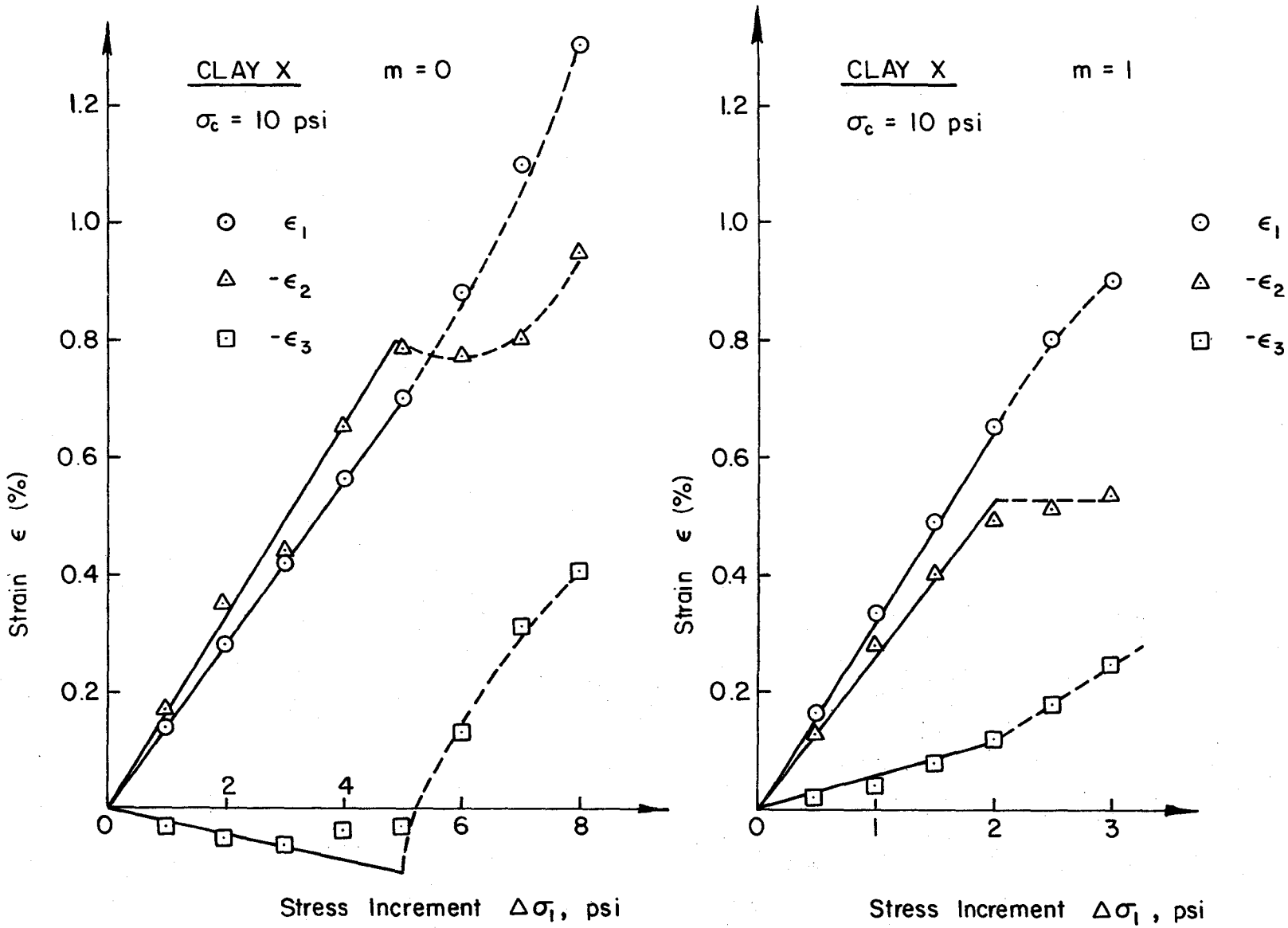

Fig. 10 Calibration of Orthotropic Material

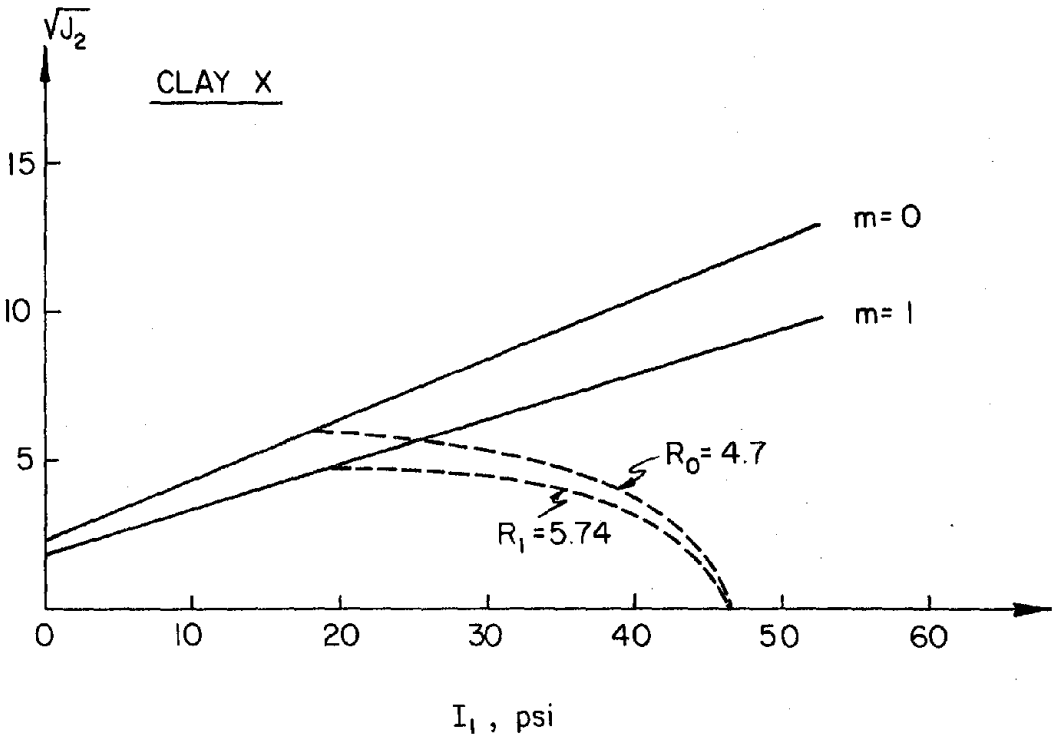

Fig. 11 Location of Hardening Caps for Clay X

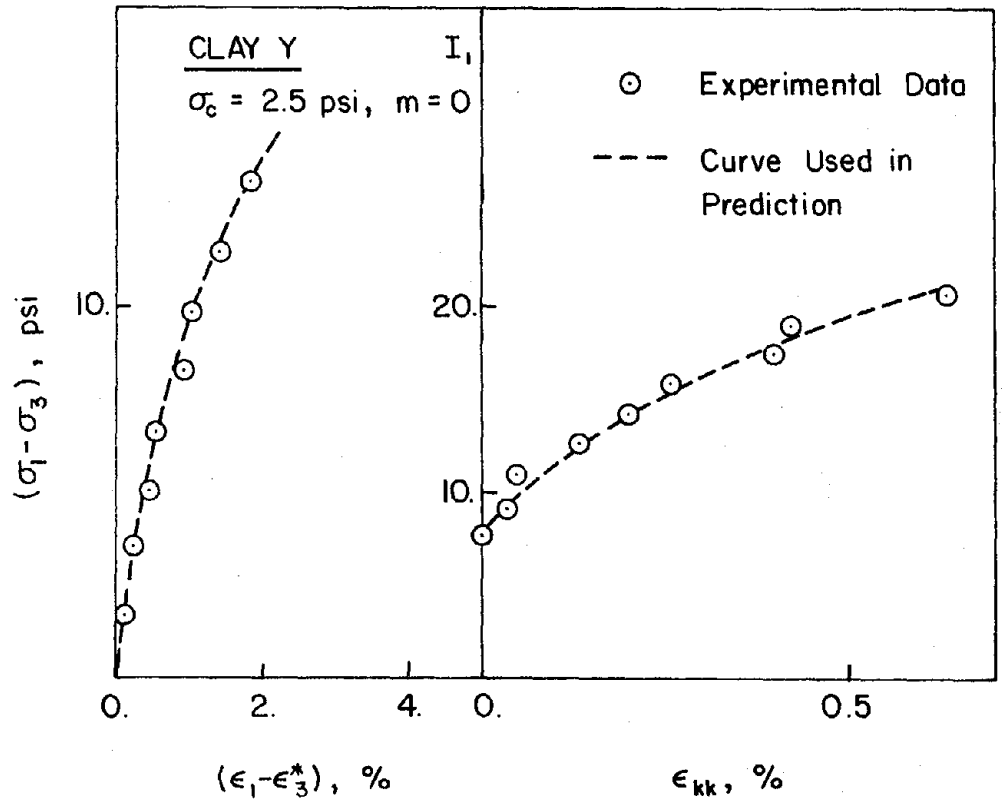

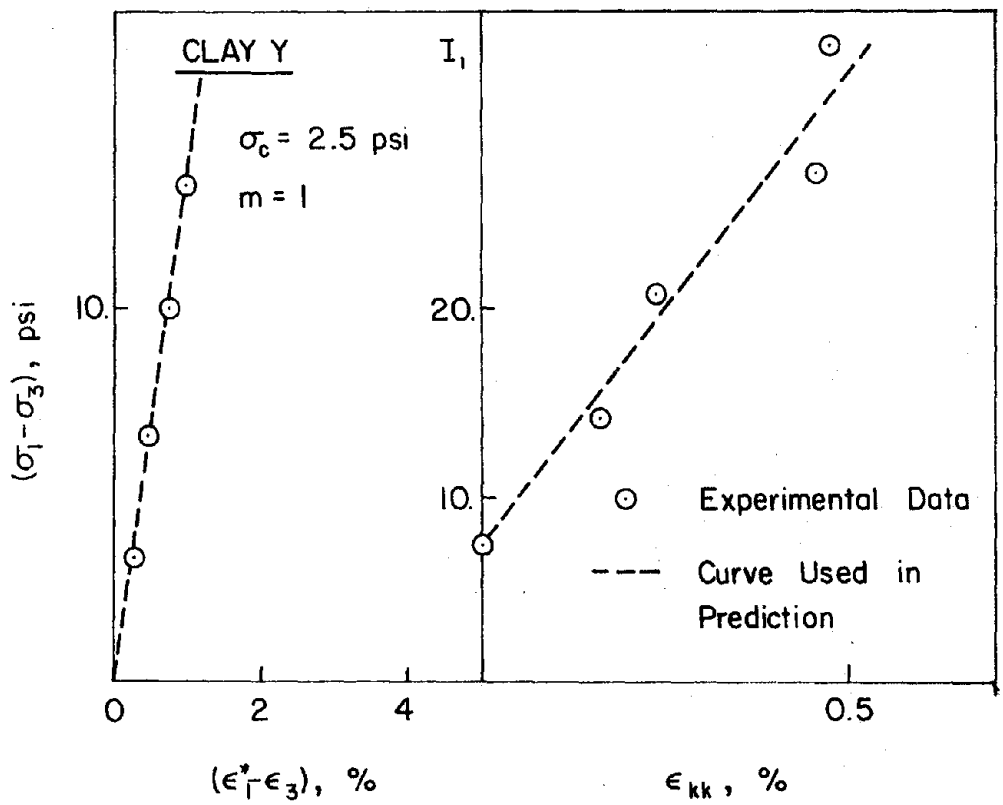

Fig. 12 Calibration of Shear and Bulk Moduli for Clay Y (σ_c = 2.5 psi, Nonlinear Elasticity Model)

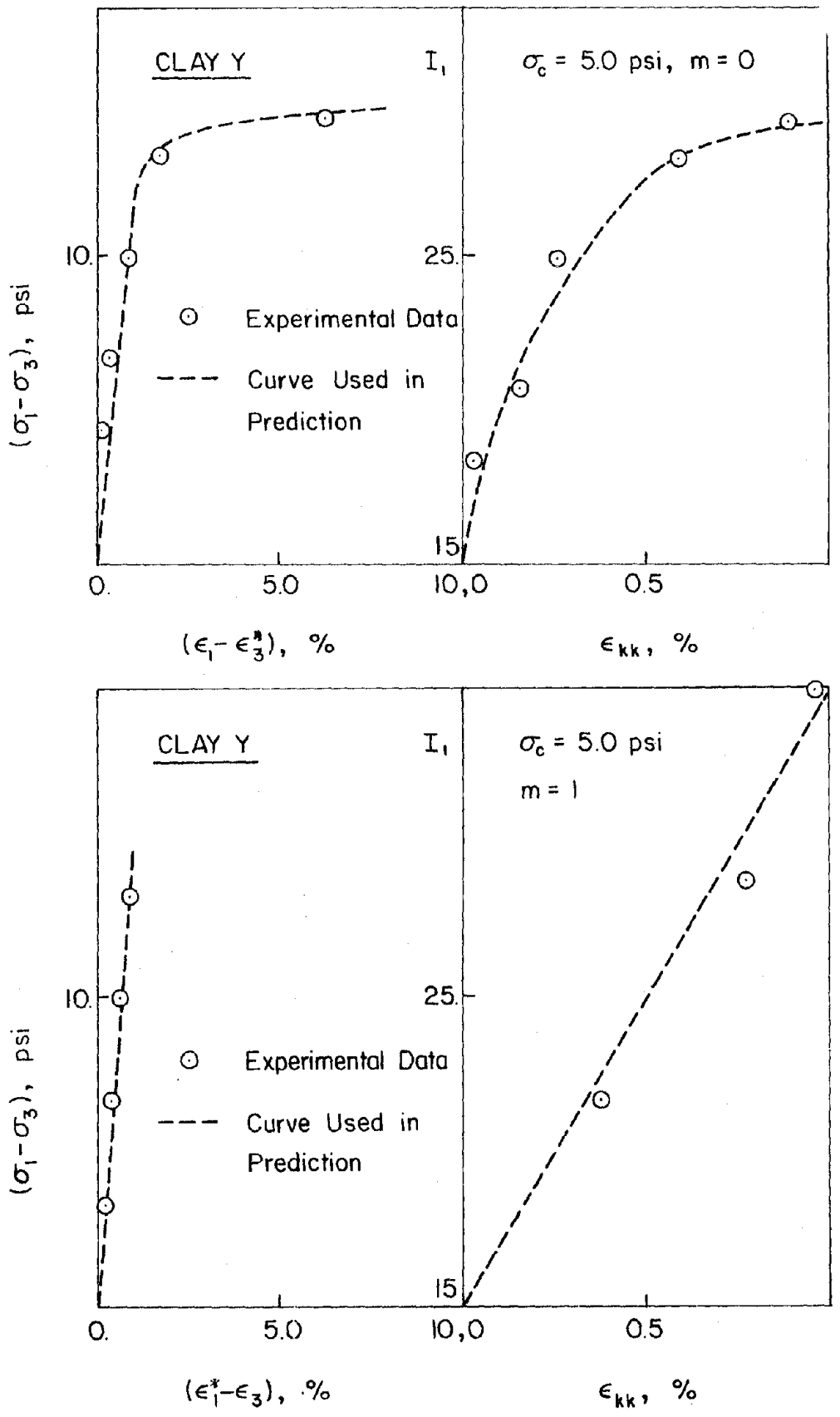

Fig. 13 Calibration of Shear and Bulk Moduli for Clay Y (σ_c = 5.0 psi, Nonlinear Elasticity Model)

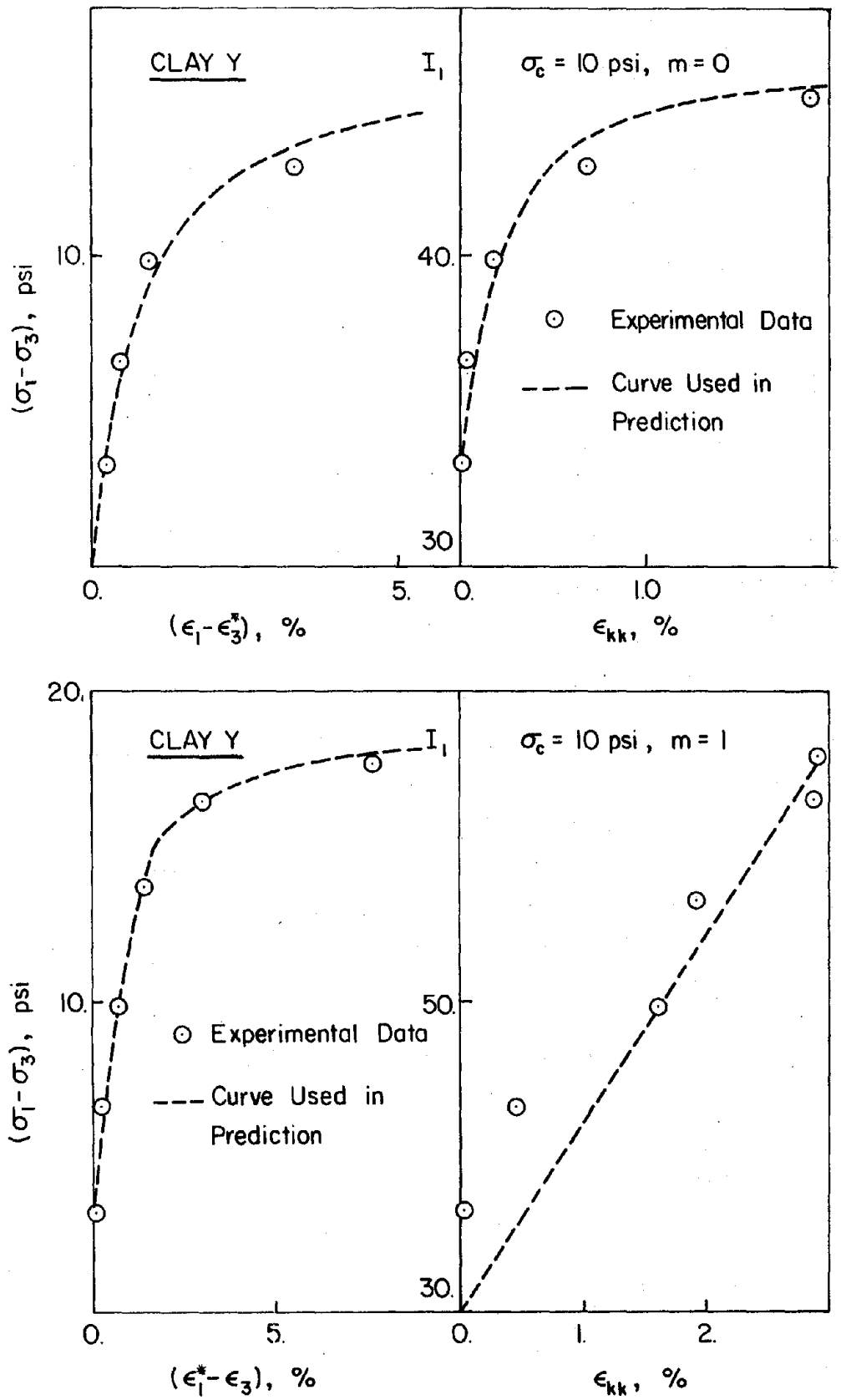

Fig. 14 Calibration of Shear and Bulk Moduli for Clay Y (σ_c = 10 psi, Nonlinear Elasticity Model)

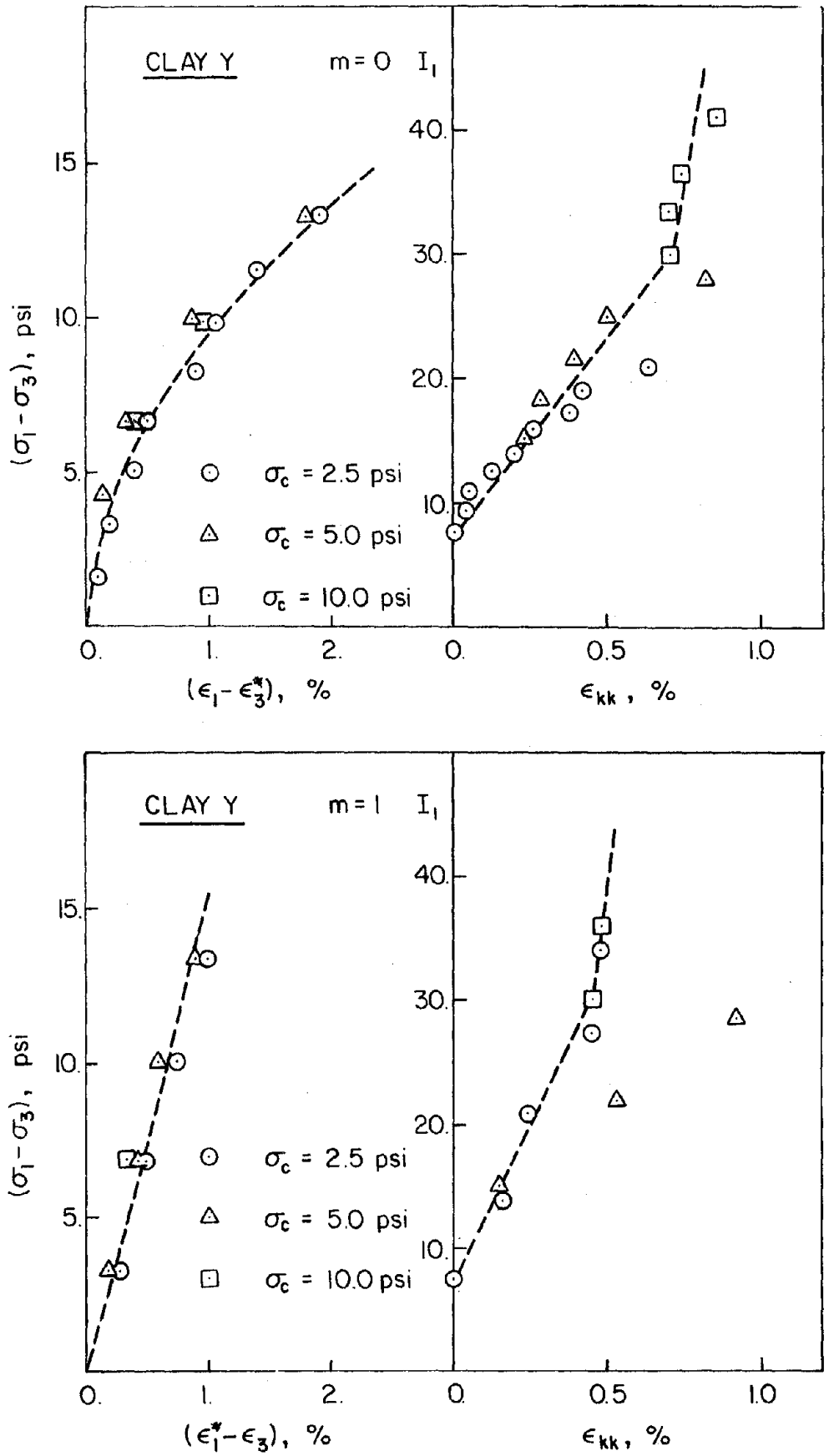

Fig. 15 Calibration of Shear and Bulk Moduli for Clay Y (Cap Model I and Cap Model II)

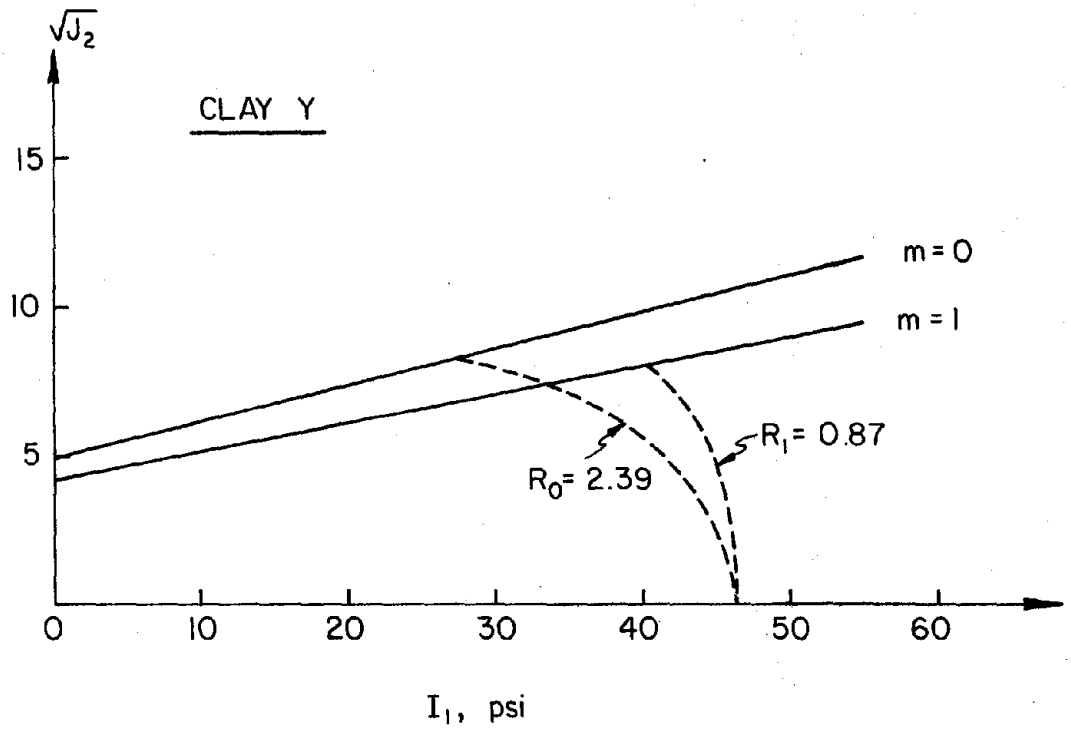

Fig. 16 Location of Hardening Caps for Clay Y

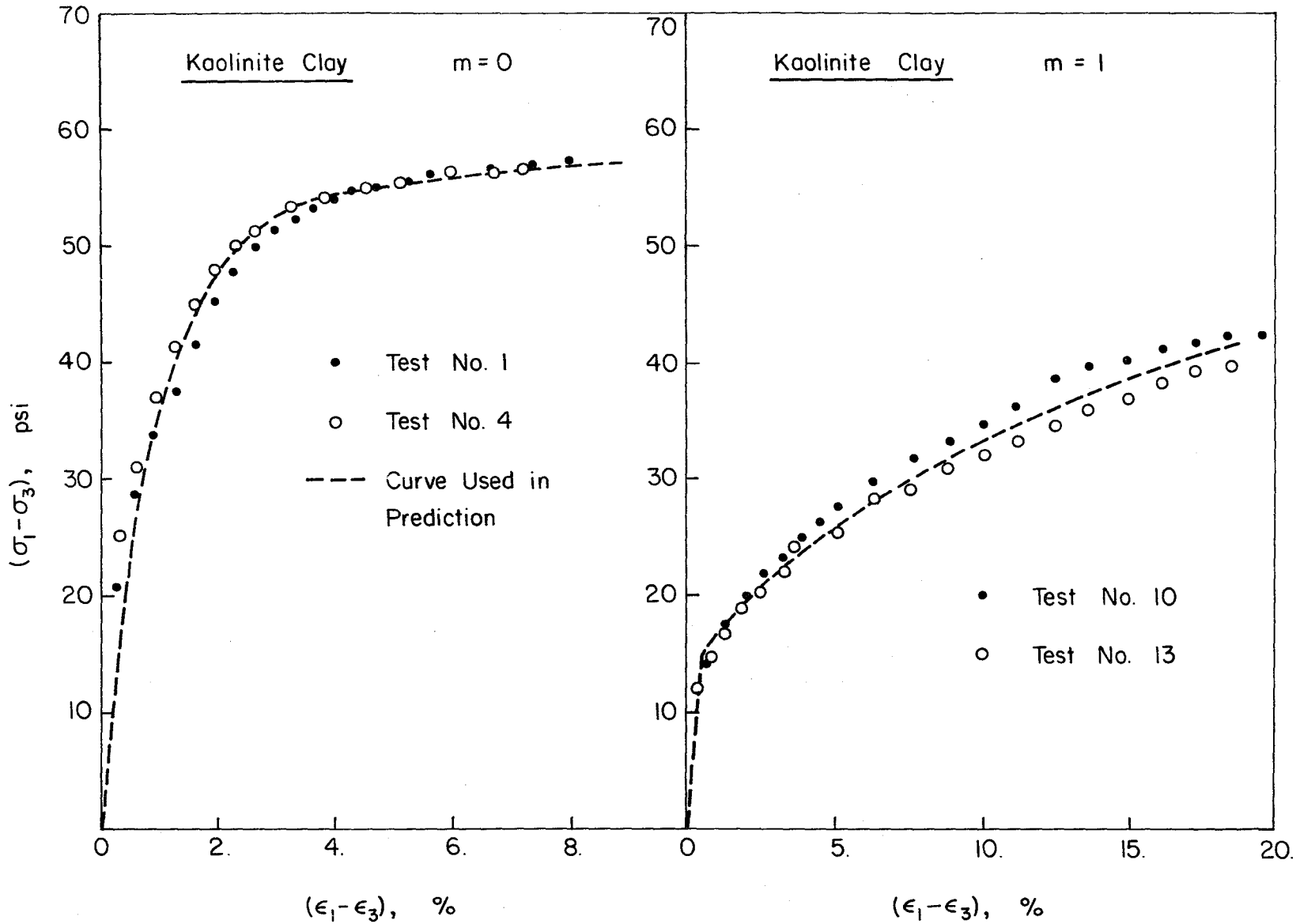

Fig. 17 Calibration of Shear Moduli for Kaolinite Clay

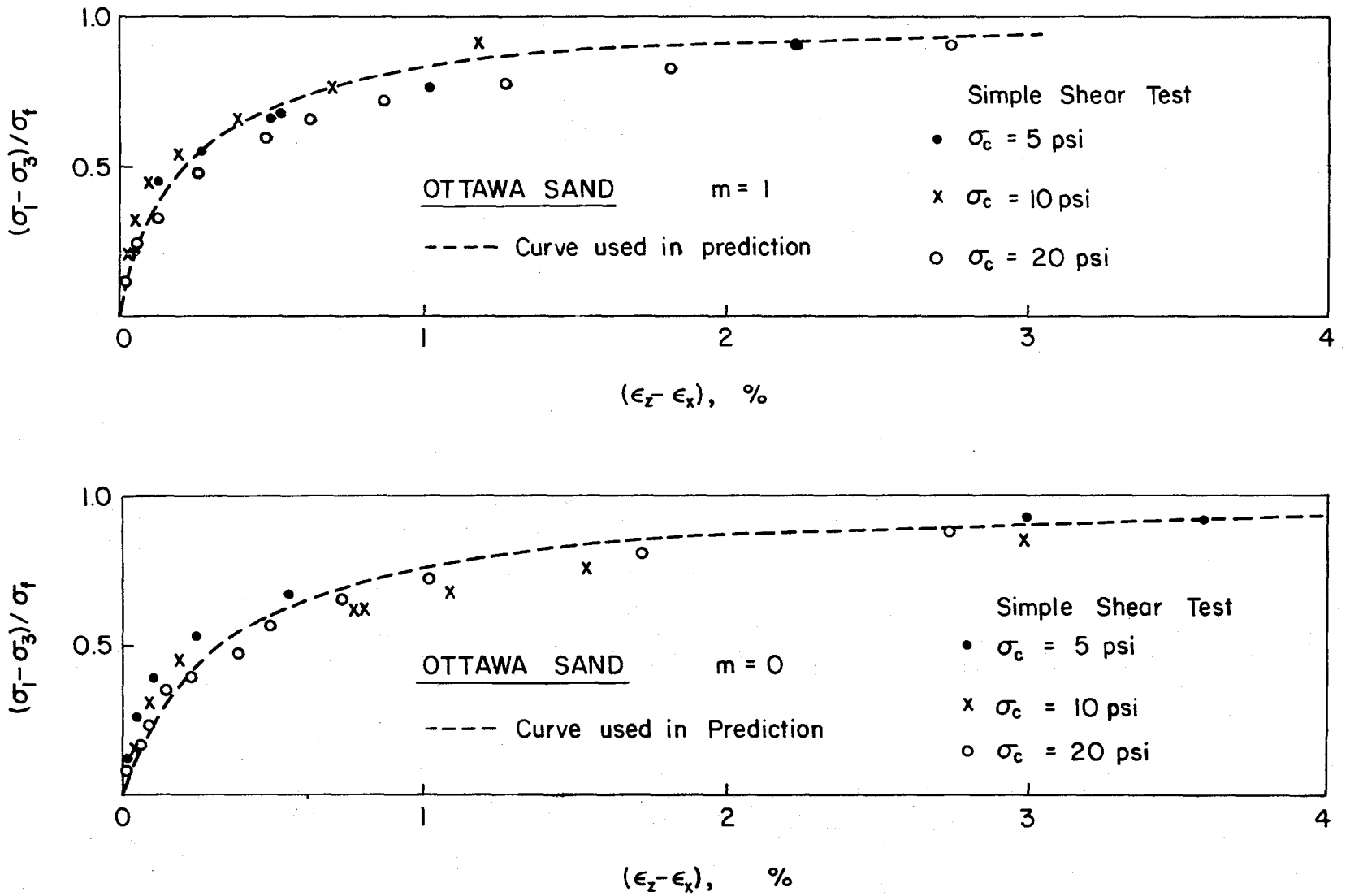

Fig. 18 Calibration of Shear Moduli for Ottawa Sand (Loading Case)

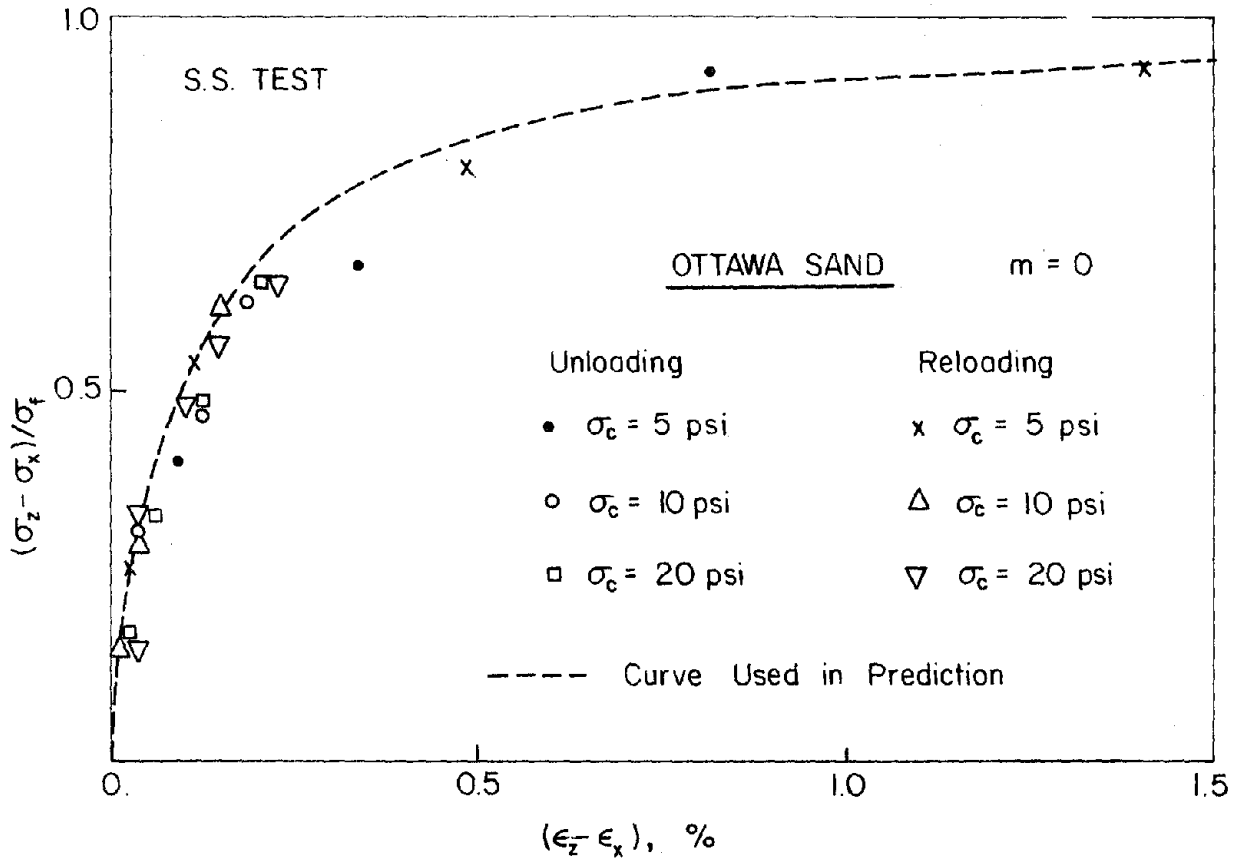

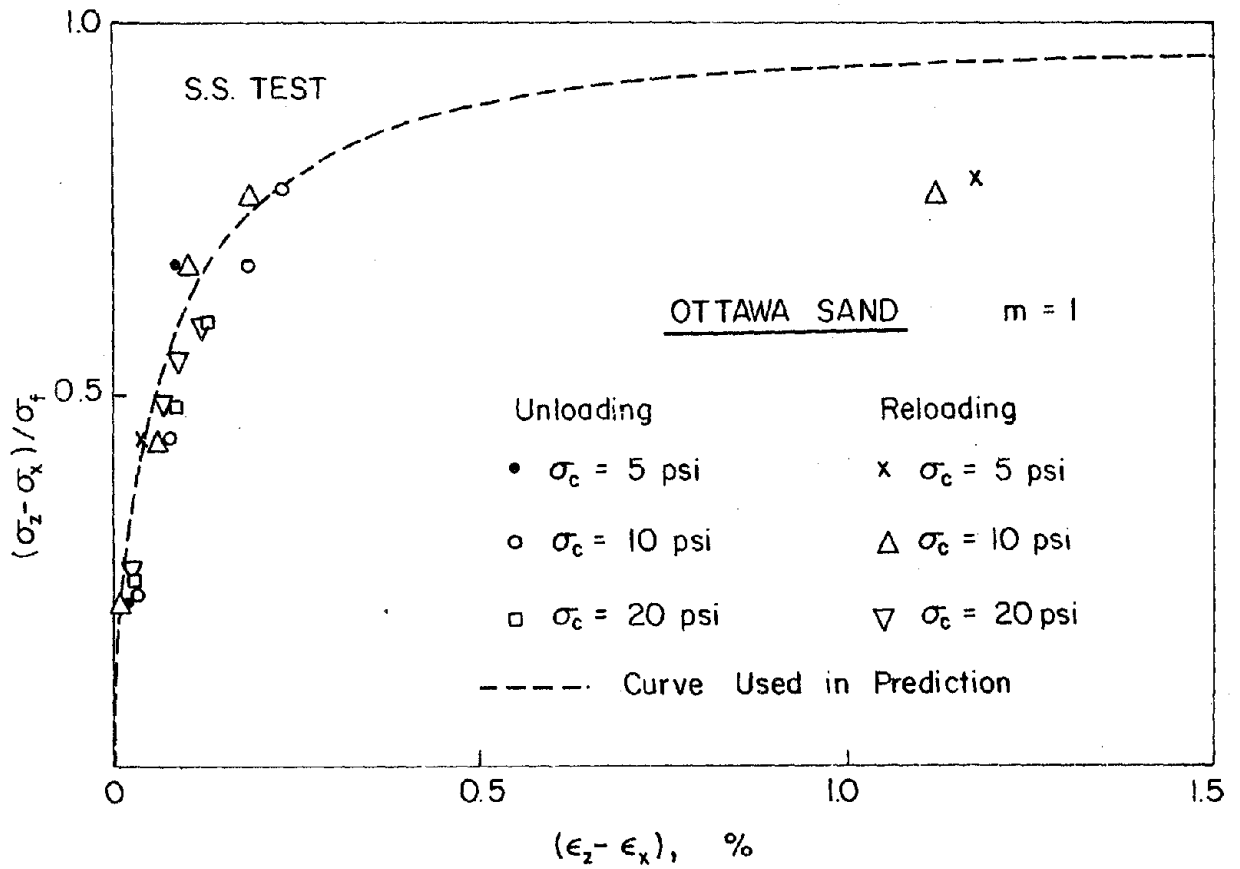

Fig. 19 Calibration of Shear Moduli for Ottawa Sand (Unloading and Reloading Cases)

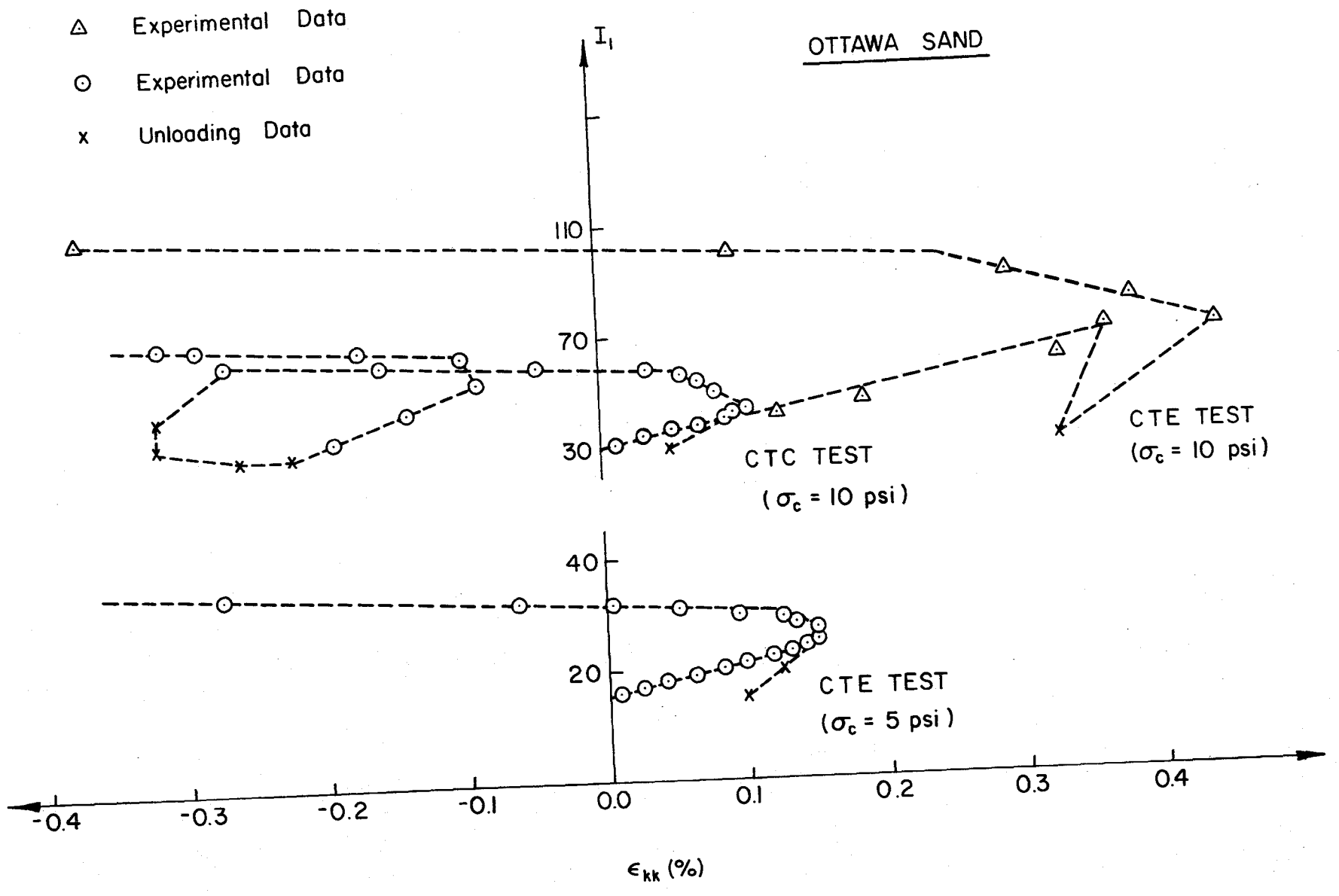

Fig. 20 Calibration of Bulk Moduli for Ottawa Sand

PLASTICITY MODELS FOR SOILS

Comparison and Discussion

by

E. Mizuno[1] and W. F. Chen[2], M. ASCE

Introduction

Herein, the predictions are made using the following three material models:

(i) Nonlinear elasticity model with the Mohr-Coulomb or the Drucker-Prager criterion as failure surface. This model is applied to all predictions.

(ii) The Mohr-Coulomb type of elastic-plastic material model with two different elliptical hardening caps. One on tensile meridian plane ($\theta = 0^\circ$) and the other on compressive meridian plane ($\theta = 60^\circ$). (Cap Model I). This model is applied to "Clay X" and "Clay Y".

(iii) The Mohr-Coulomb type of elastic-plastic material model with a three-dimensional elliptical cap whose shape depends on the Lode angle θ . (Cap Model II). This model is applied to "Clay X" and "Clay Y".

The comparison and discussion are given in the forthcoming.

Clay X

The comparison of the predictions with the experimental data on the simple shear tests with constant mean stresses at 10 psi, 20 psi and

[1]Research Assistant, School of Civil Engineering, Purdue University, West Lafayette, IN 47907

[2]Professor of Structural Engineering, School of Civil Engineering, Purdue University, West Lafayette, IN 47907

30 psi are presented in Figs. 1 through 4 for each of the stress ratio m = 0.25, 0.5, 0.75. In these figures, the stress difference-axial strain relation, and the axial strain-volumetric strain relation are presented. The experimental data are shown by the open circles and the predictions are denoted by lines.

As can be seen from the figures, the predictions by the nonlinear elasticity model are off somewhat from the experimental data with σ_c = 20 psi and 30 psi. The model, however, gives a good prediction for the tests with σ_c = 10 psi and for σ_c = 30 psi, m = 0.75. Since the model is assumed to be isotropic, it is difficult to predict the behavior of the anisotropic clay X. Also, it should be noted that the volumetric strain ε_v on the simple shear tests can not be predicted by this model.

Cap models are seen to predict the axial strain-stress difference relation and the axial strain-volumetric strain relation well for all experiments shown in figures. The tests at σ_c = 10 psi show elastic. In the prediction (σ_c = 10 psi), the cap models show some plastic strains in the region near failure surface. For the experiment with σ_c = 10 psi, m = 0.5, the cap model I predicts only elastic strains because the decomposed stresses do not reach the hardening caps. Therefore, there is no plastic strains.

Clay Y

The comparison of prediction with experimental data on the triaxial tests under initial confining pressures σ_c = 2.5, 5.0 and 10 psi is presented in Figs. 5 through 7 for each of the stress ratio m = 0.25, 0.5, 0.75. As the initial confining pressures lie on the swelling line, clay Y behaves first like an elastic material in the tests. Nonlinear elasticity model predicts well the experiments with σ_c = 2.5 and 5.0 psi. However, the predictions for the tests with σ_c = 10 psi, m = 0.5 and σ_c = 10 psi, m = 0.75 are off somewhat from the actual data. This implies that plastic strains must occur in the tests. Cap models reflect this as shown in Fig. 7. The predictions by cap models for the triaxial tests with σ_c = 2.5 psi and 5 psi are almost the same as that of nonlinear elasticity model. For these cases, either the stress paths have not reached the hardening caps, or the plastic strains are small at this stage of loading.

Kaolinite Clay

The comparison of the predictions with the data on the triaxial or simple shear tests under the undrained condition is presented in Figs. 8 through 12. The total axial stress vs. axial strain curves are shown in the figures. As can be seen, the nonlinear elasticity model predicts the experiments well. In particular, the predictions for Test NO. 7, 8, 9, 11 and 12 are very good. In this model, the pore water pressure increment is taken to be equivalent to the increment of the first invariant of the stress tensor I_1.

Ottawa Sand

The comparison of predictions with experimental data on various tests is presented in Figs. 13 through 21. In each figure, the strains in x, y and z directions are plotted against the octahedral shear stress τ_{oct}. Except the circular stress path, all predictions are good. In particular, the initial slope of the actual behavior of Ottawa sand and the failure load are accurately predicted by the nonlinear elasticity model combined with the Mohr-Coulomb criterion. As for the circular stress path, the model prediction is different significantly from the actual data in the region of Lode angle θ between 60° and 420° (Fig. 21).

Acknowledgments

This material is based upon work supported by the National Science Foundation under Grant No. PFR-7809326 to Purdue University.

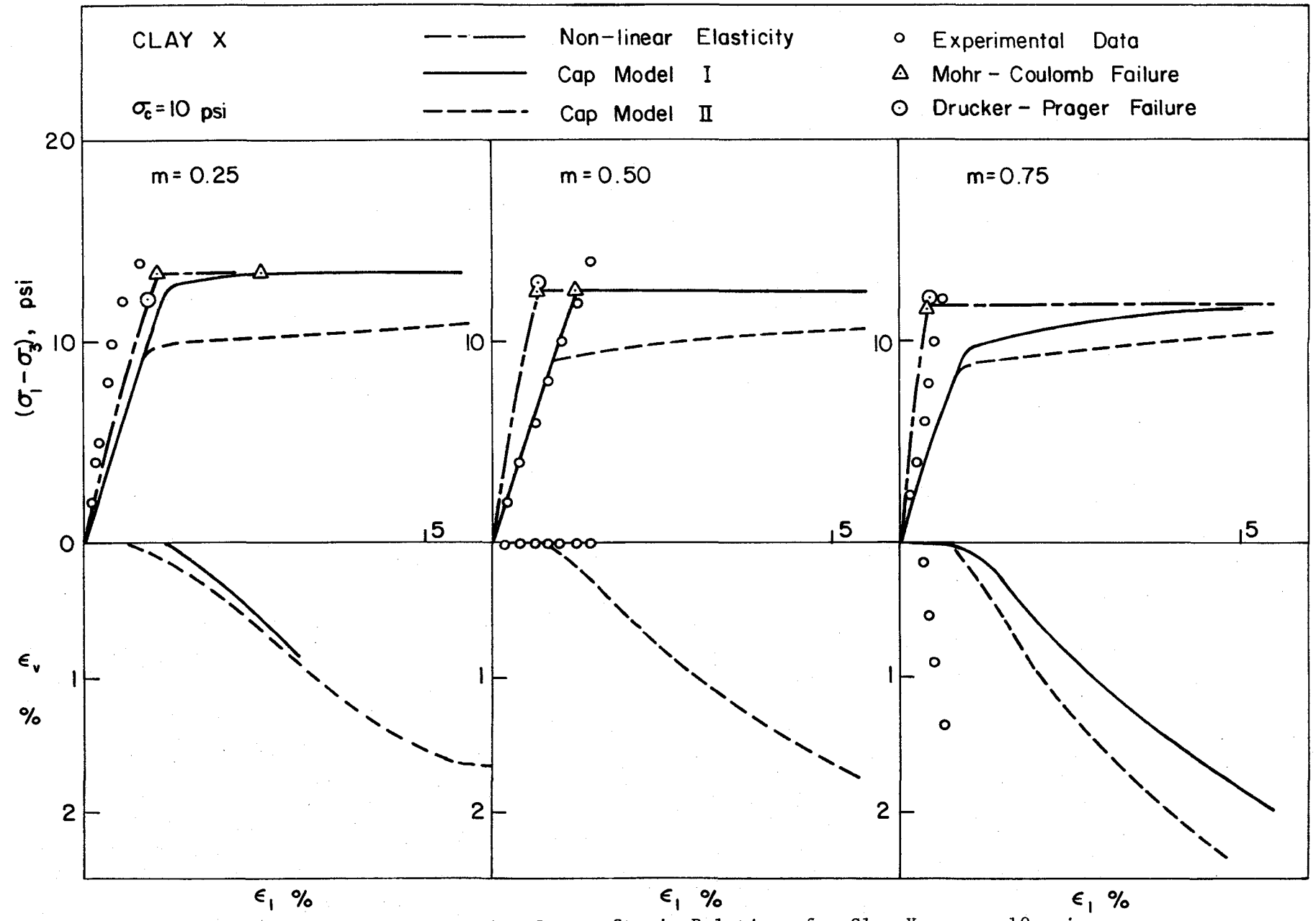

Fig. 1 Stress-Strain Relations for Clay X, σ_c = 10 psi

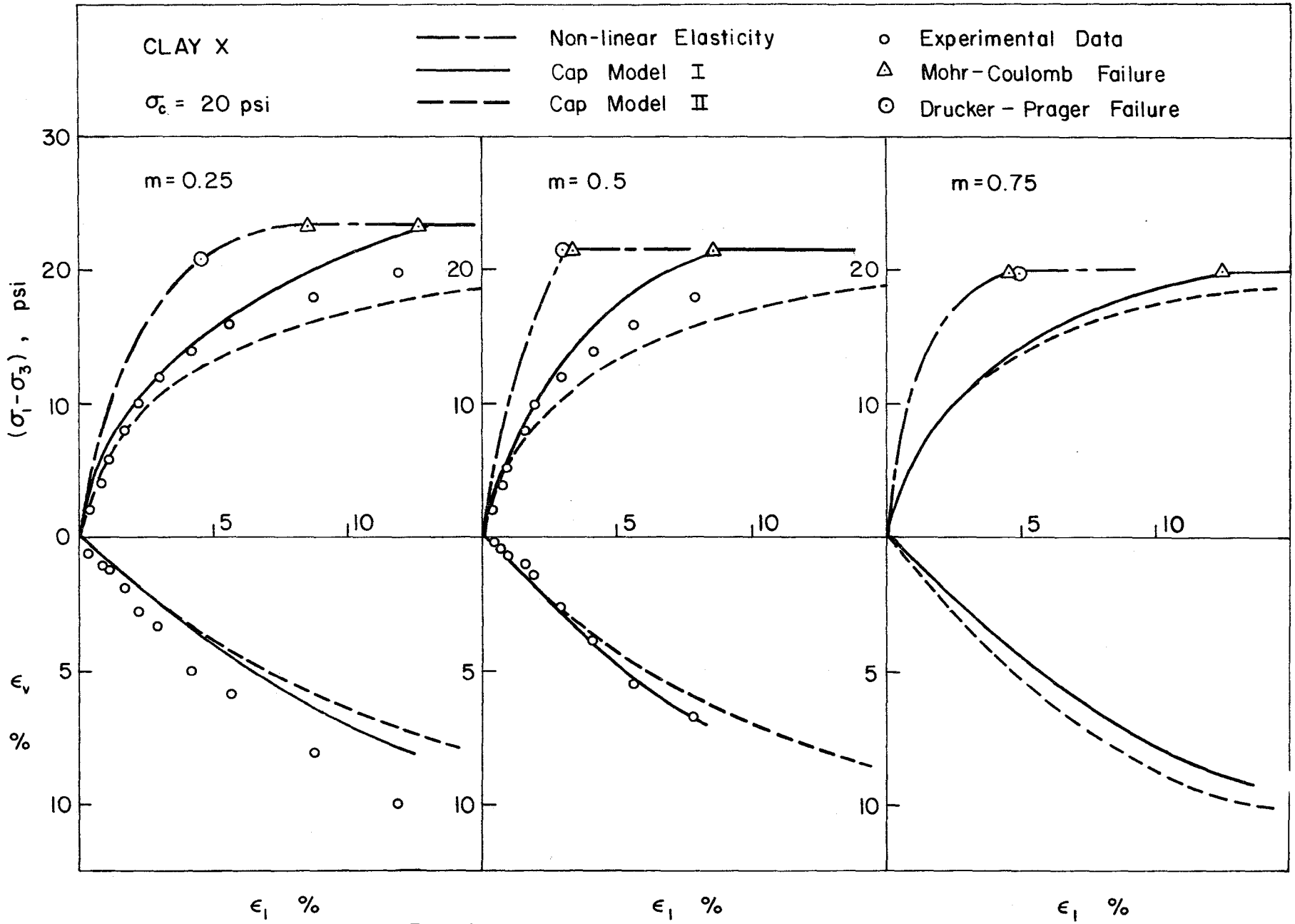

Fig. 2 Stress-Strain Relations for Clay X, σ_c = 20 psi

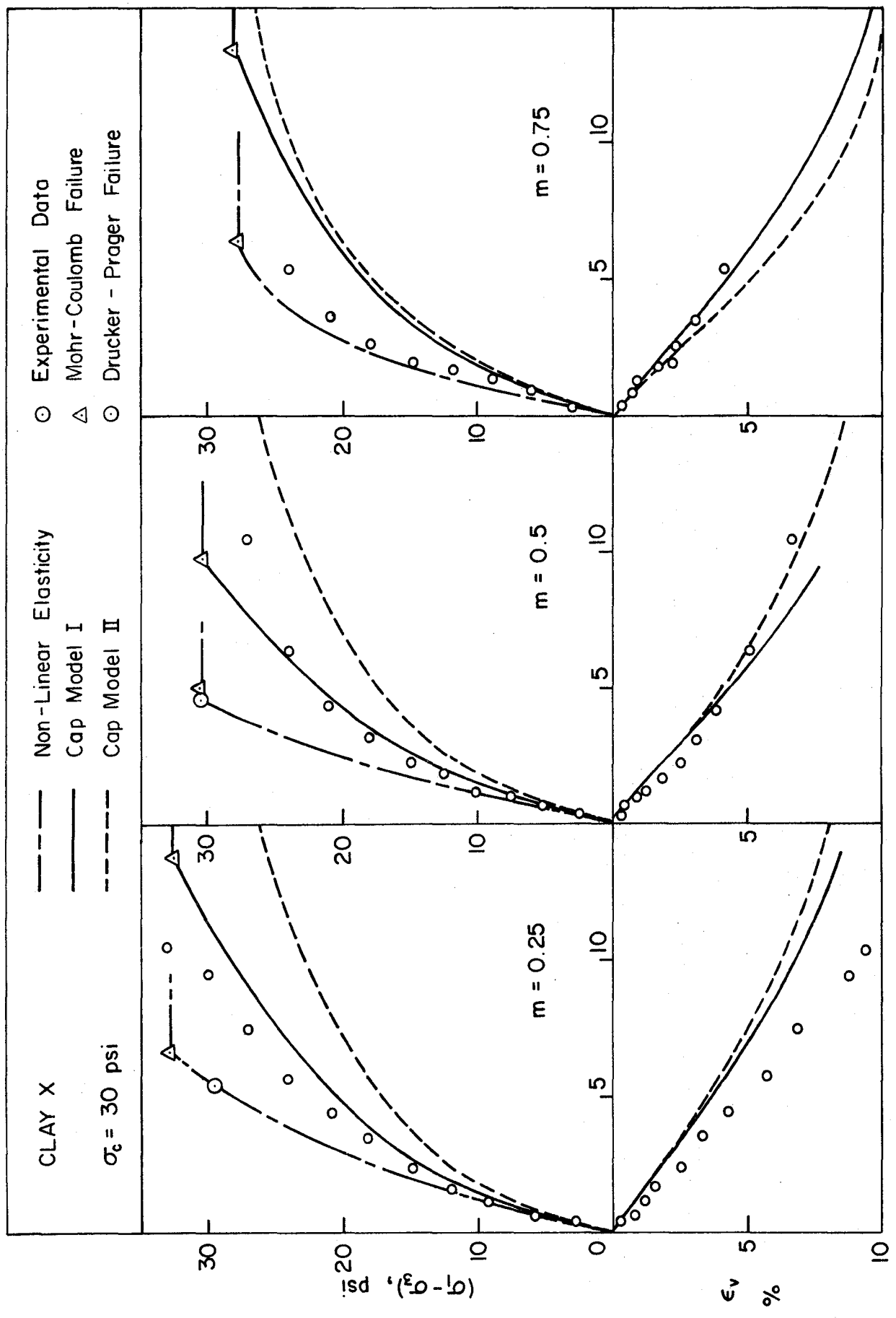

Fig. 3 Stress-Strain Relations for Clay X, σ_c = 30 psi

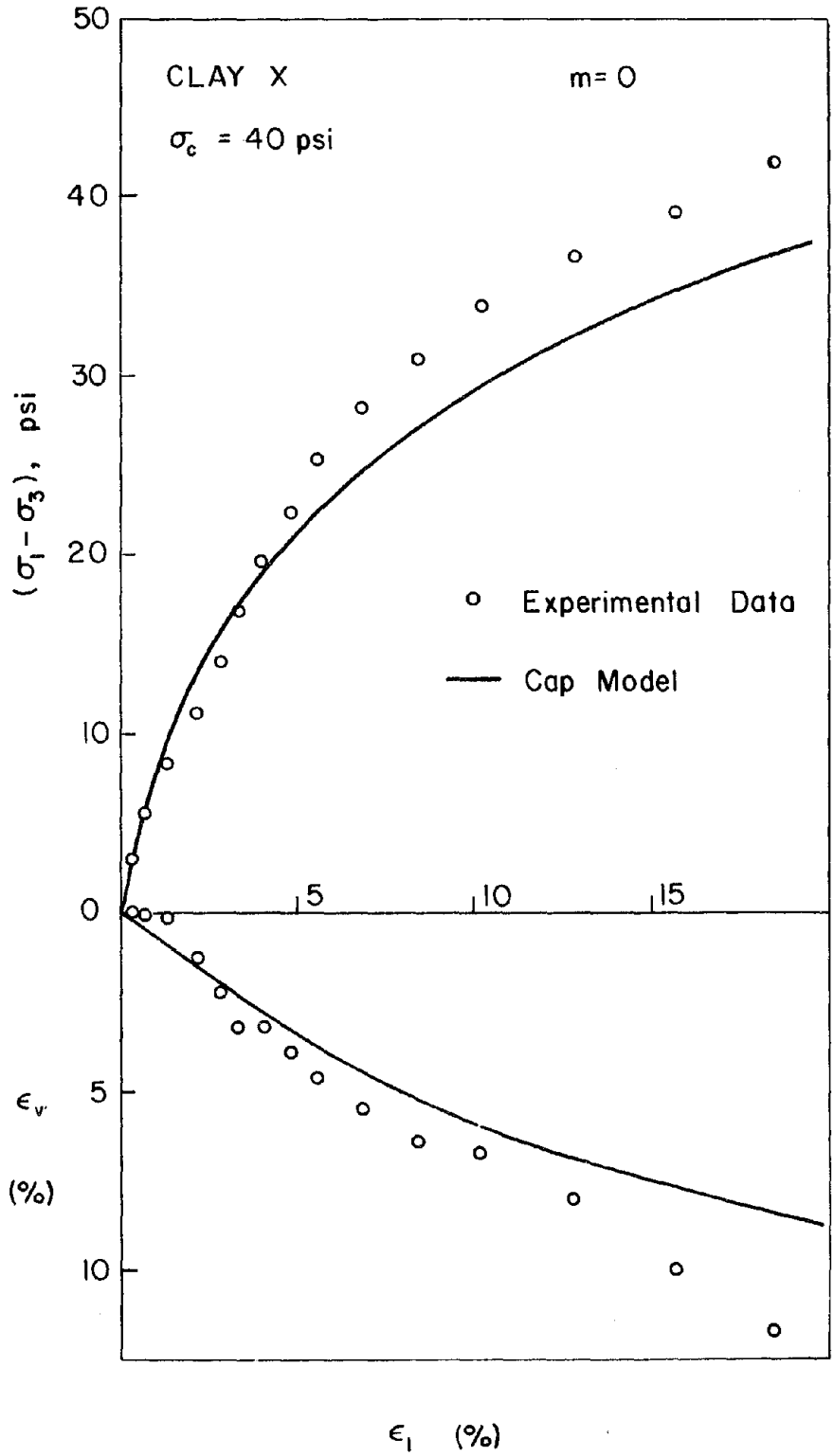

Fig. 4 Stress-Strain Relations for Clay X, σ_c = 40 psi

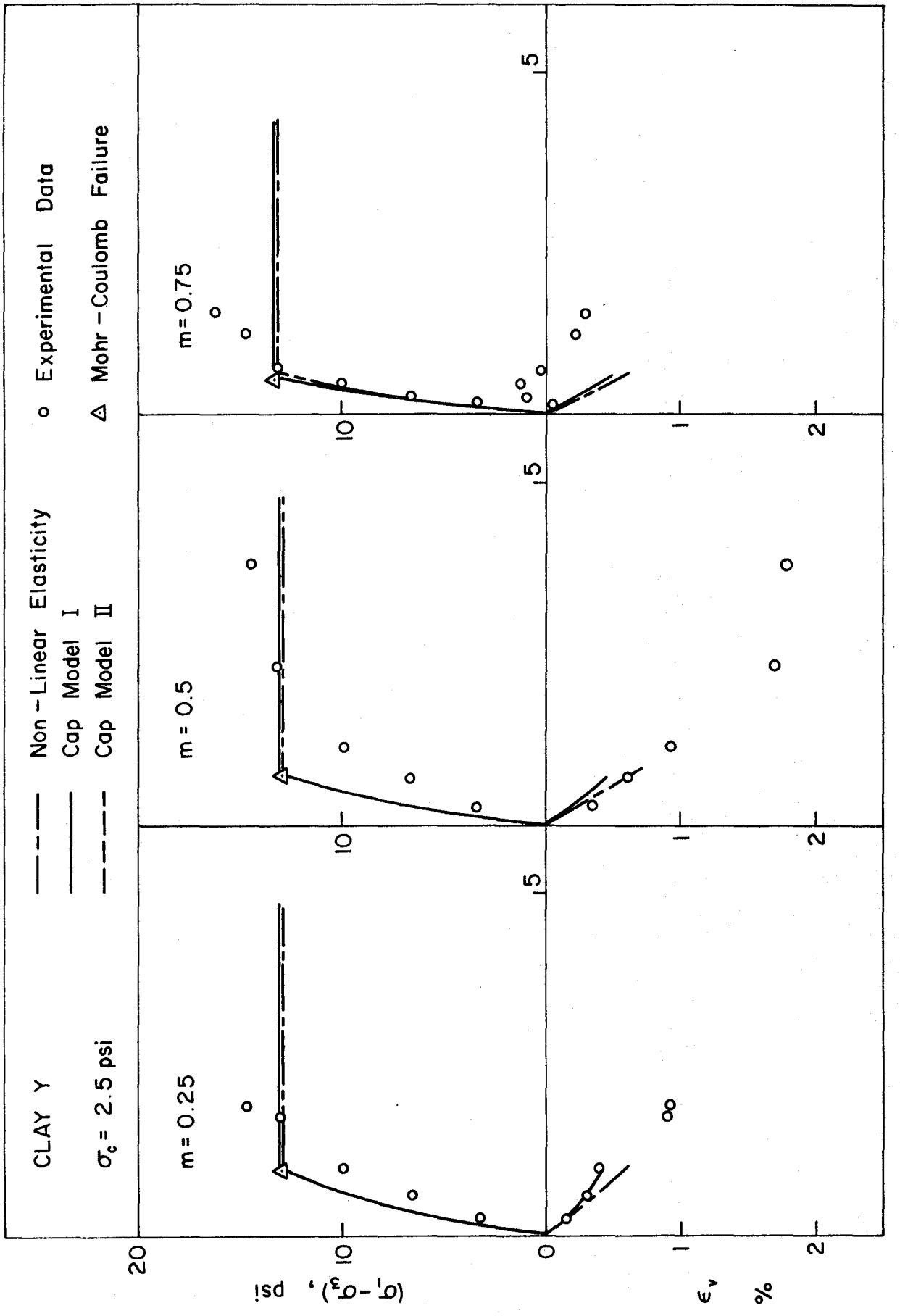

Fig. 5 Stress-Strain Relations for Clay Y, σ_c = 2.5 psi

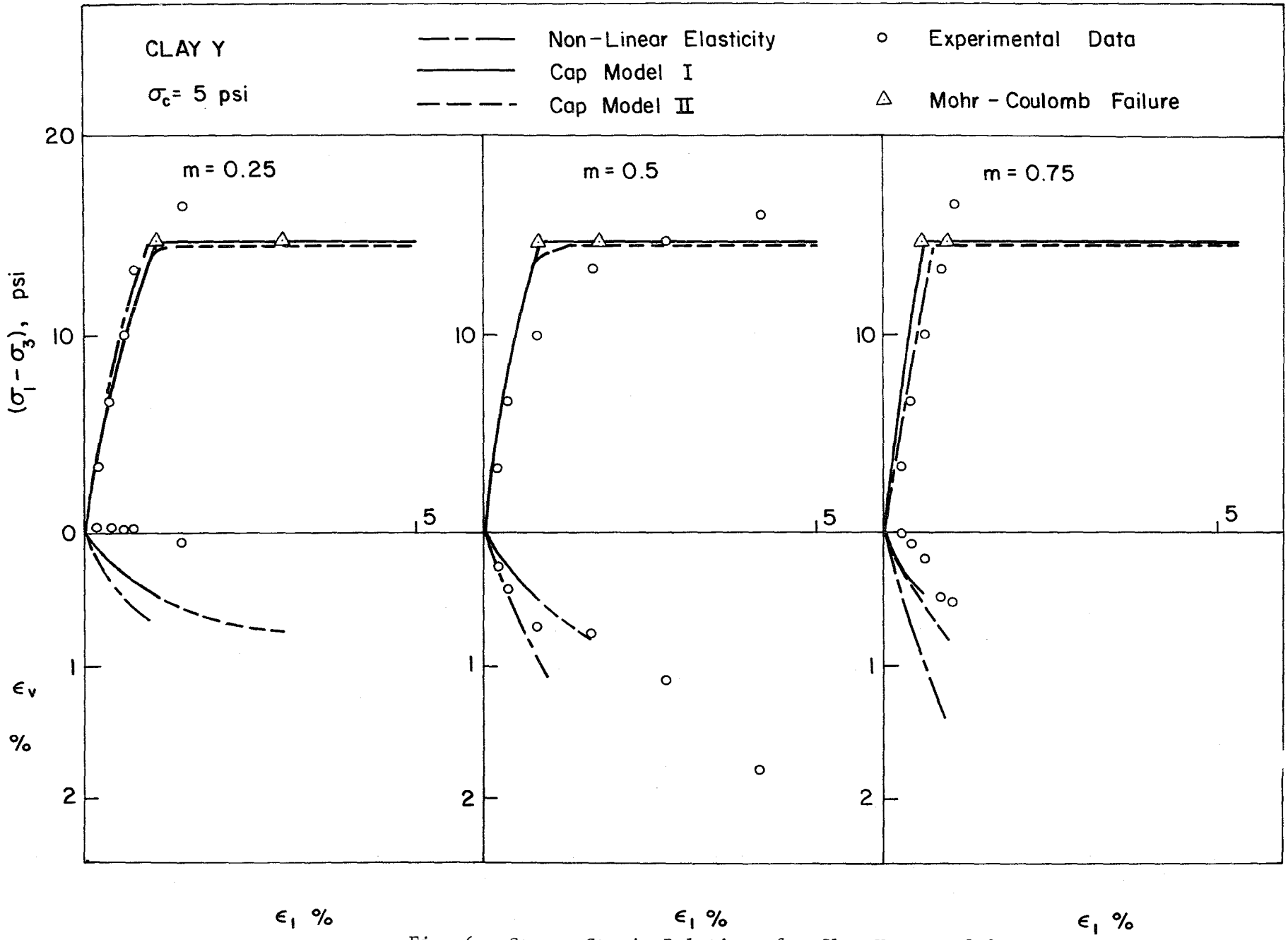

Fig. 6 Stress-Strain Relations for Clay Y, σ_c = 5.0 psi

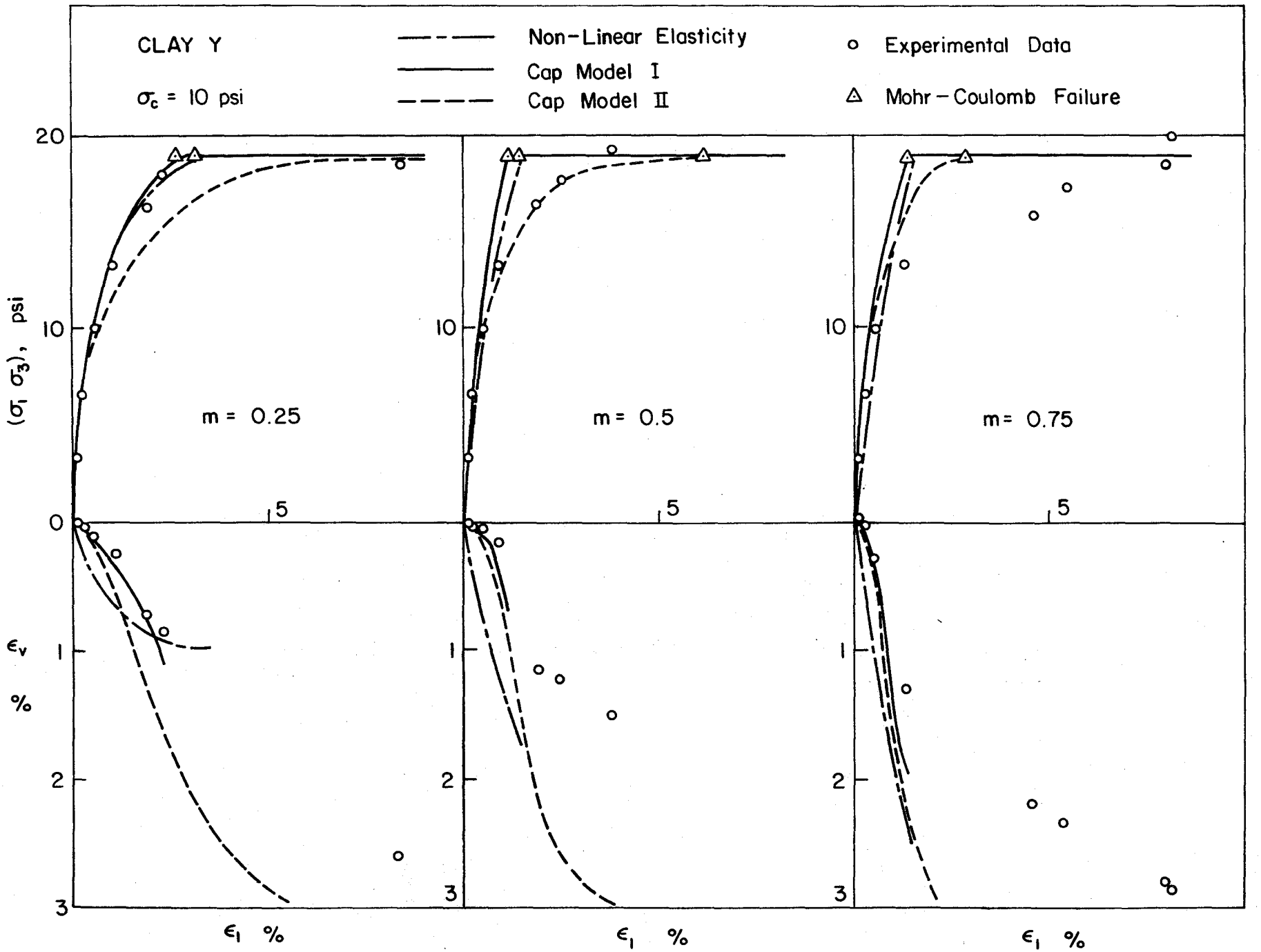

Fig. 7 Stress-Strain Relations for Clay Y, σ_c = 10 psi

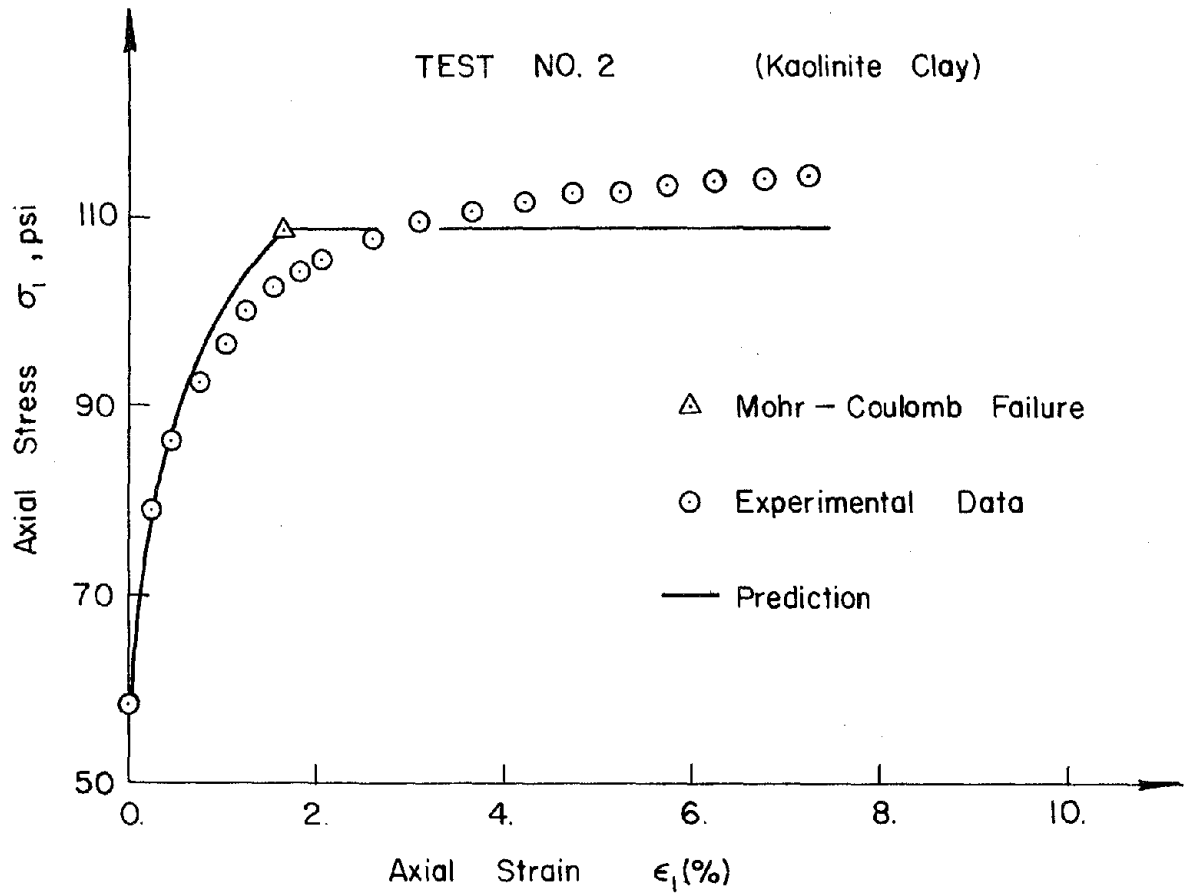

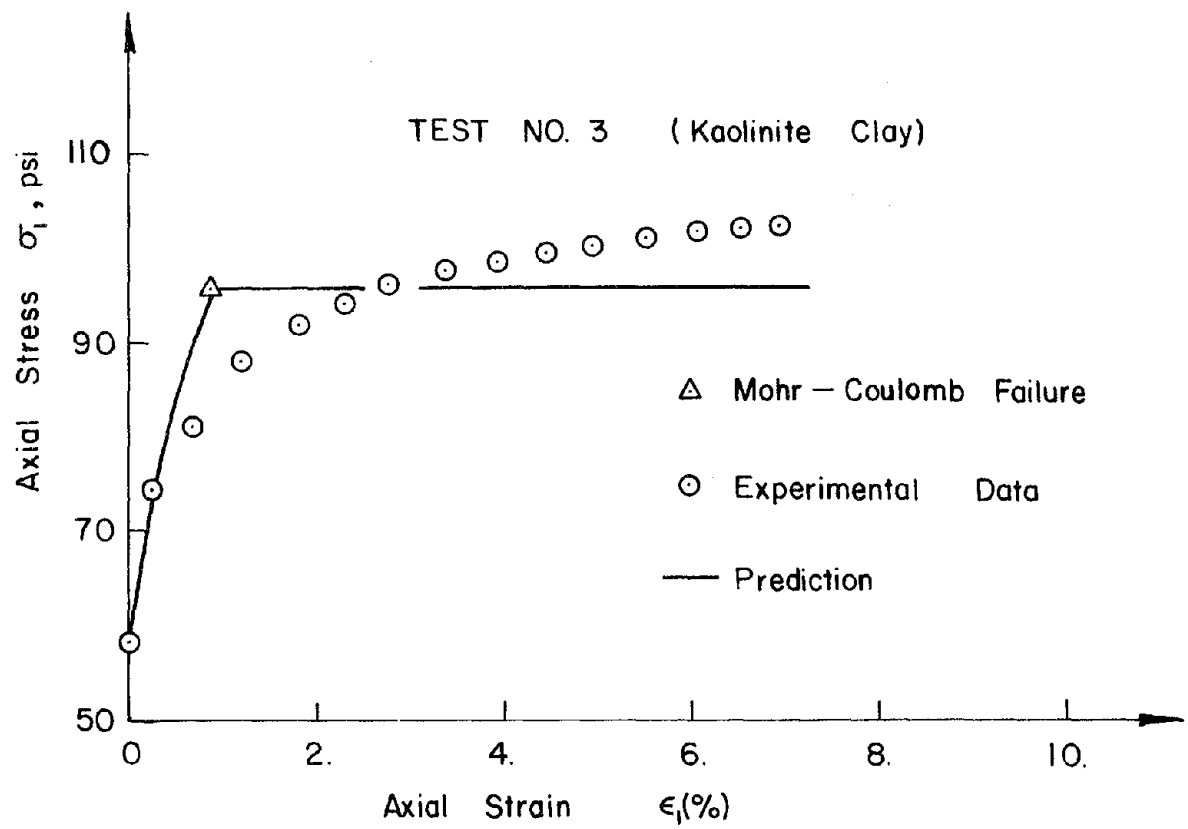

Fig. 8 Axial Stress-Strain Relations for Kaolinite Clay, Test No. 2 and 3

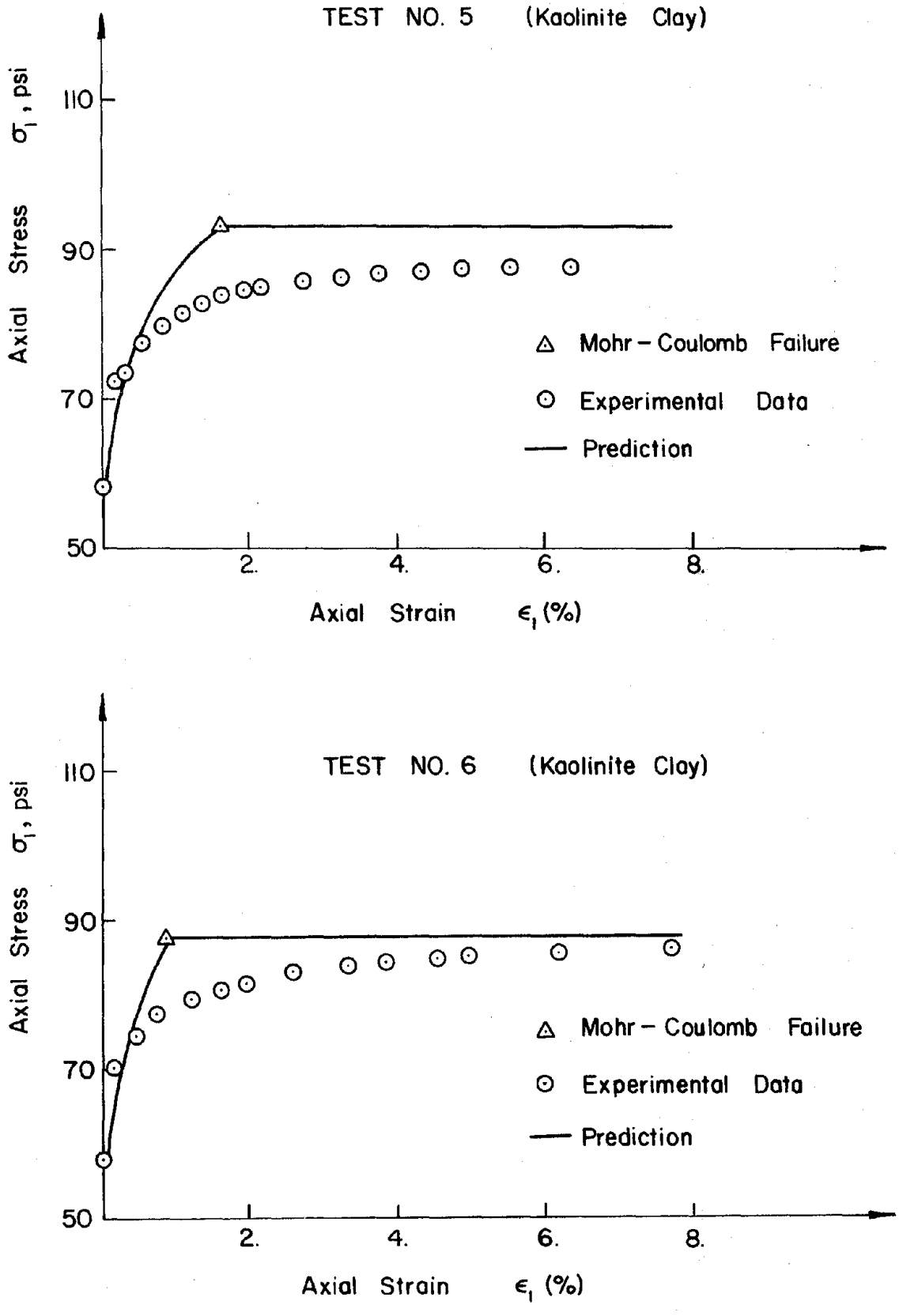

Fig. 9 Axial Stress-Strain Relations for Kaolinite Clay, Test No. 5 and 6

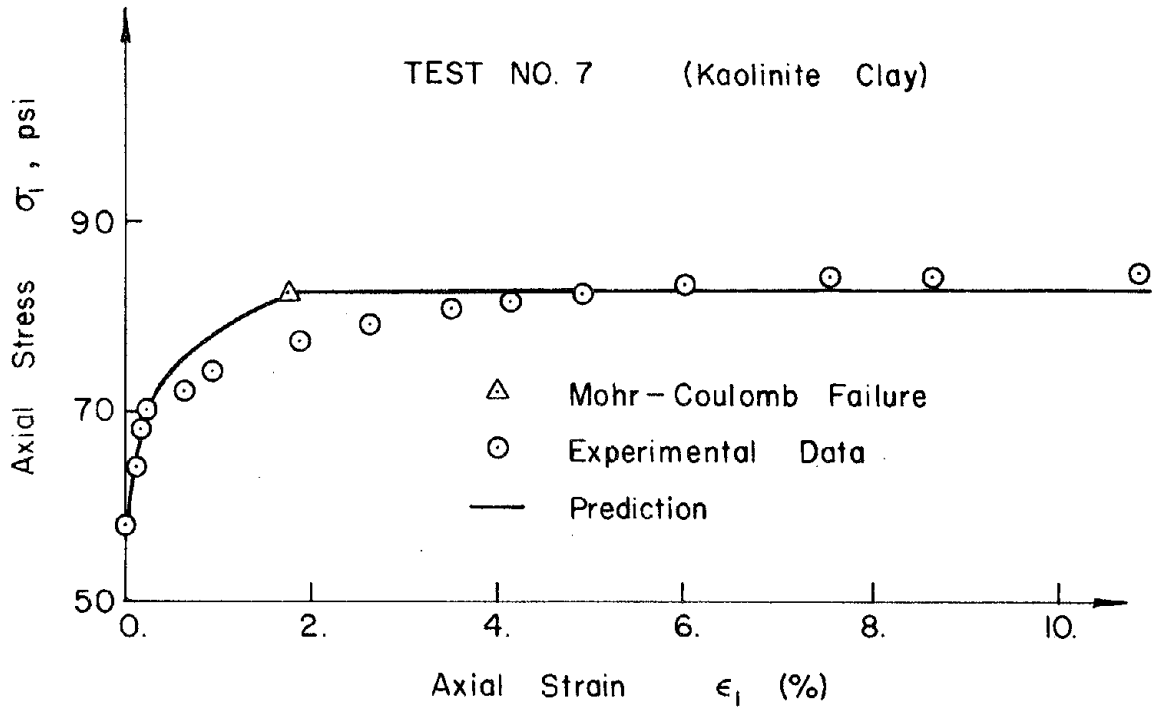

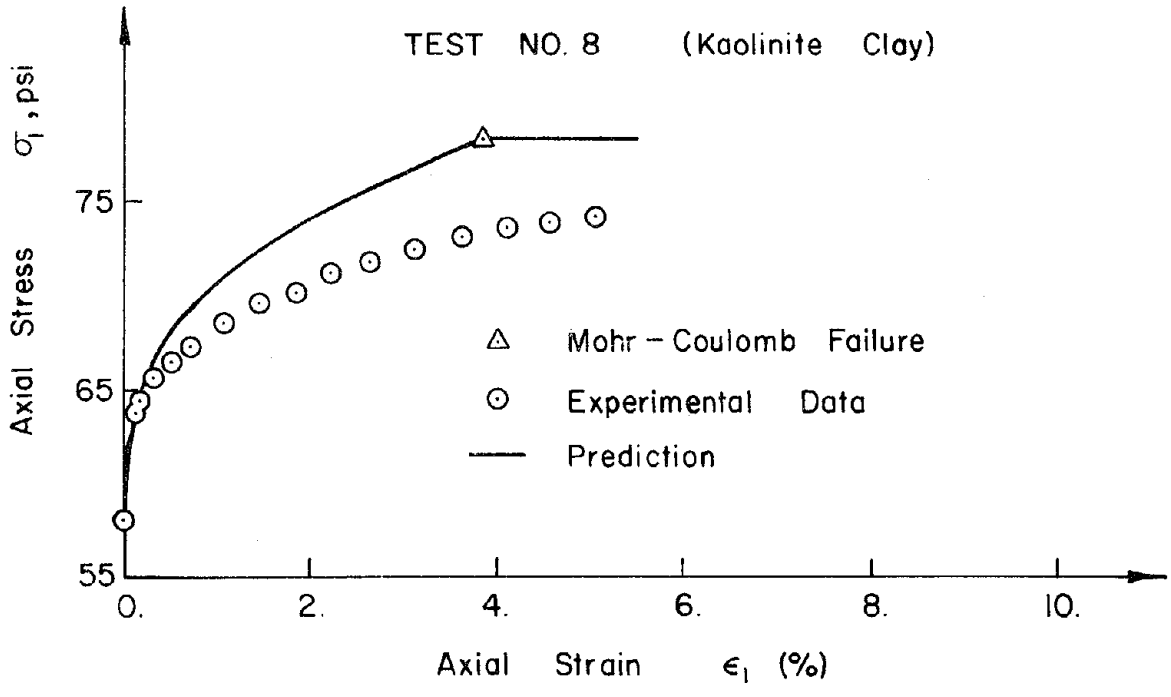

Fig. 10 Axial Stress-Strain Relations for Kaolinite Clay, Test No. 7 and 8

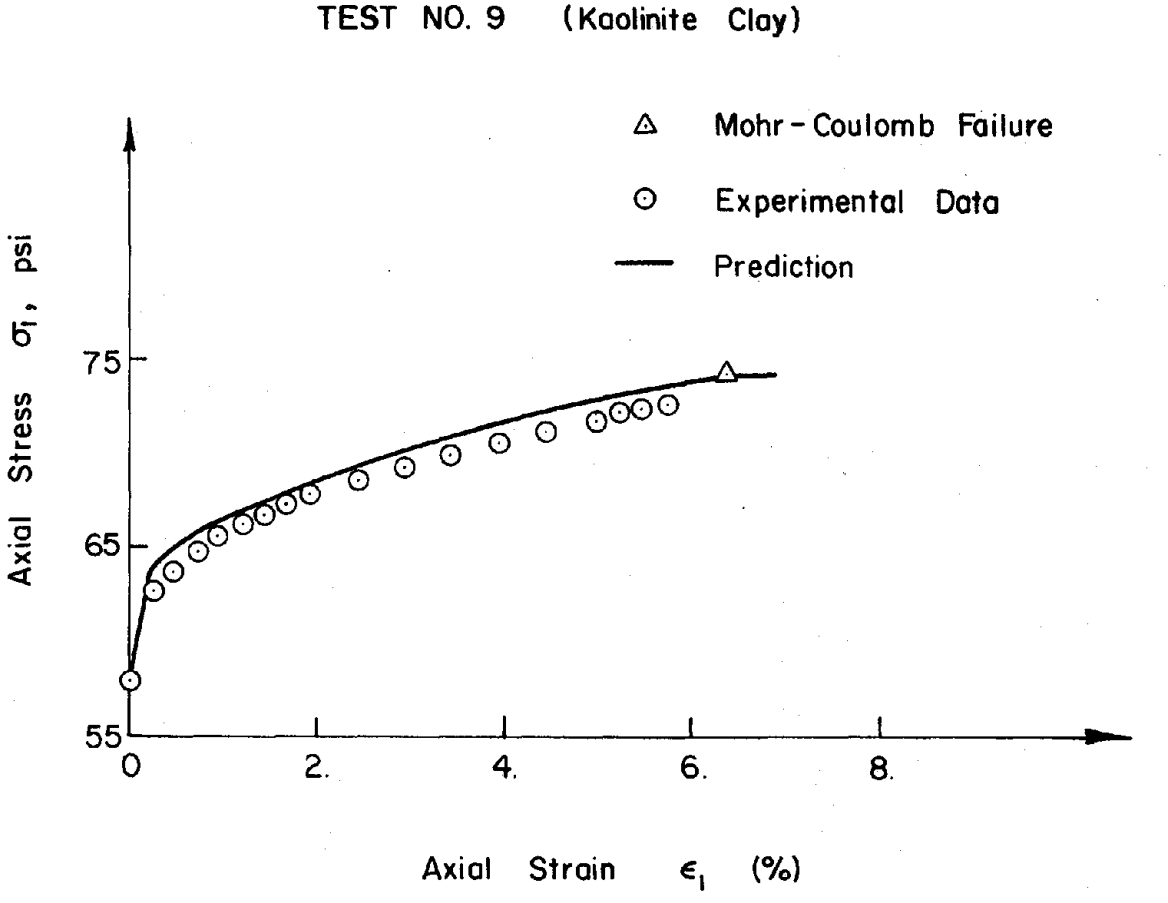

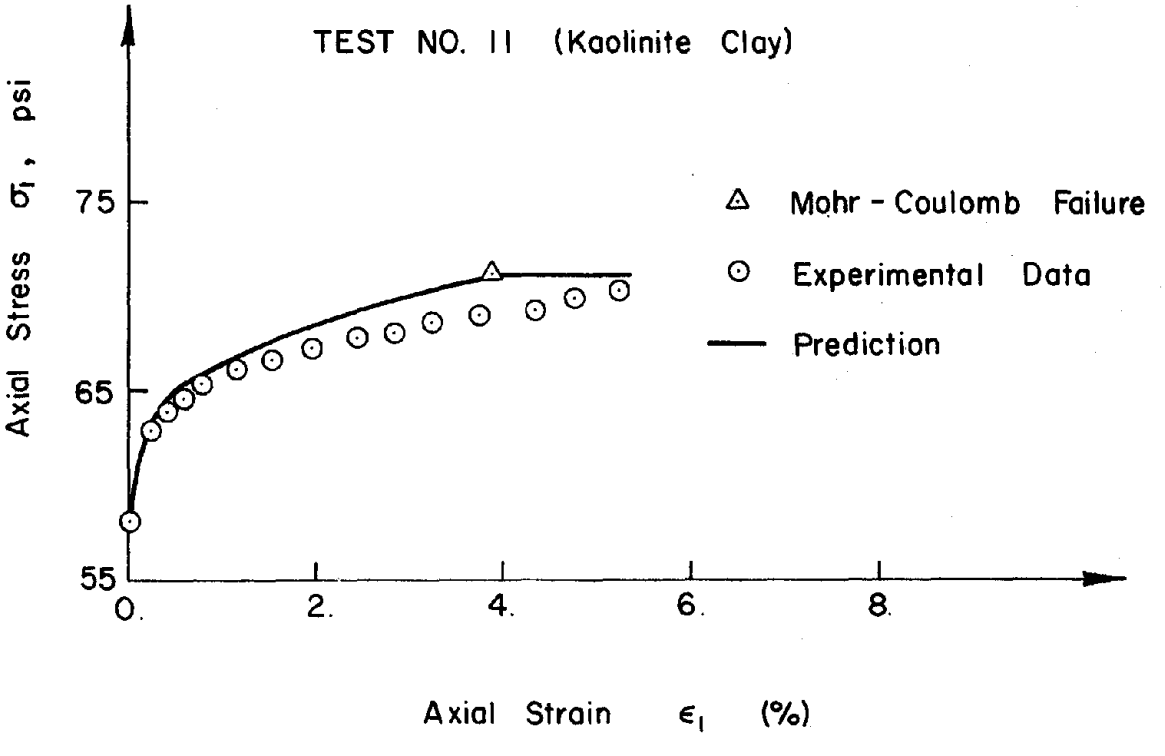

Fig. 11 Axial Stress-Strain Relations for Kaolinite Clay, Test No. 9 and 11

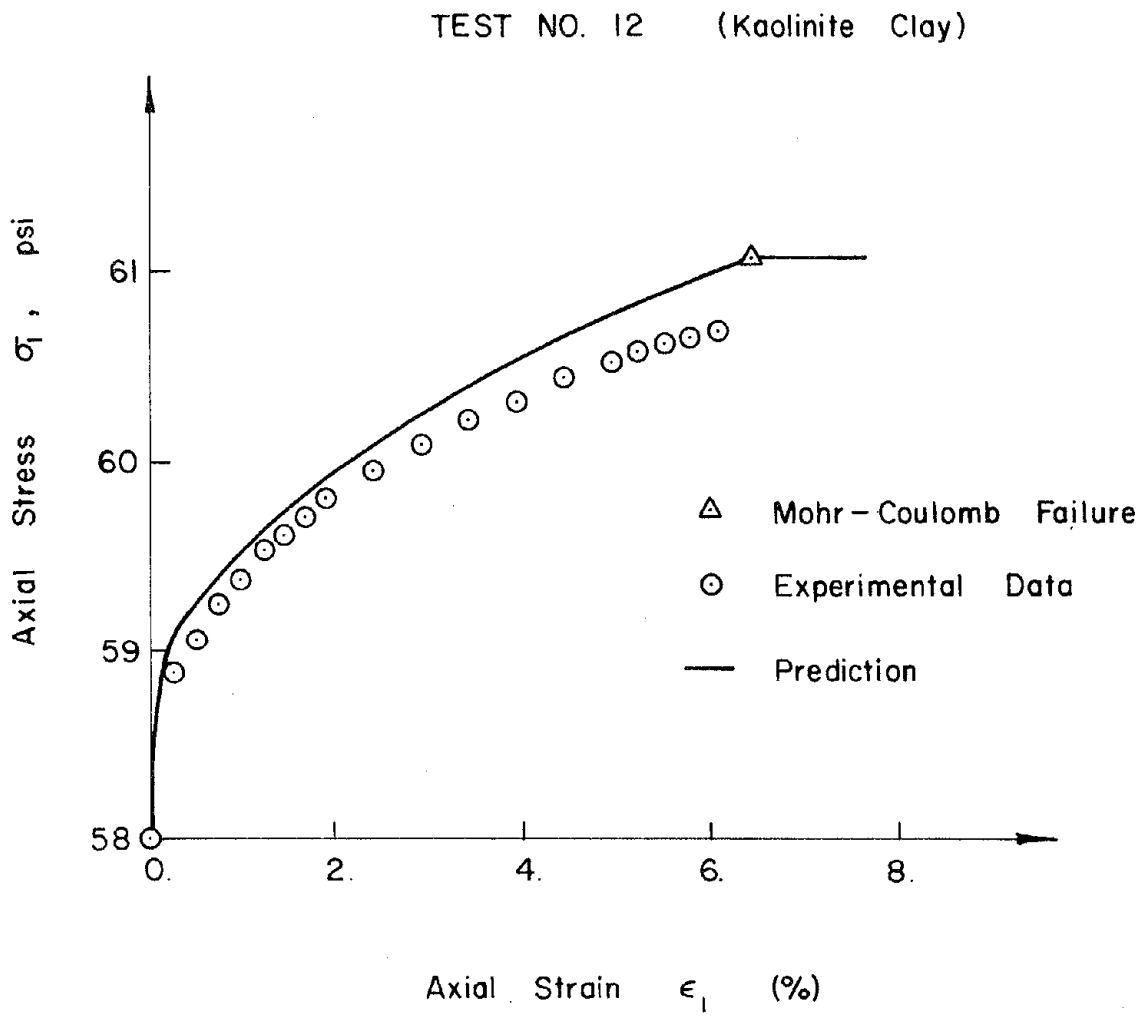

Fig. 12 Axial Stress-Strain Relation for Kaolinite Clay, Test No. 12

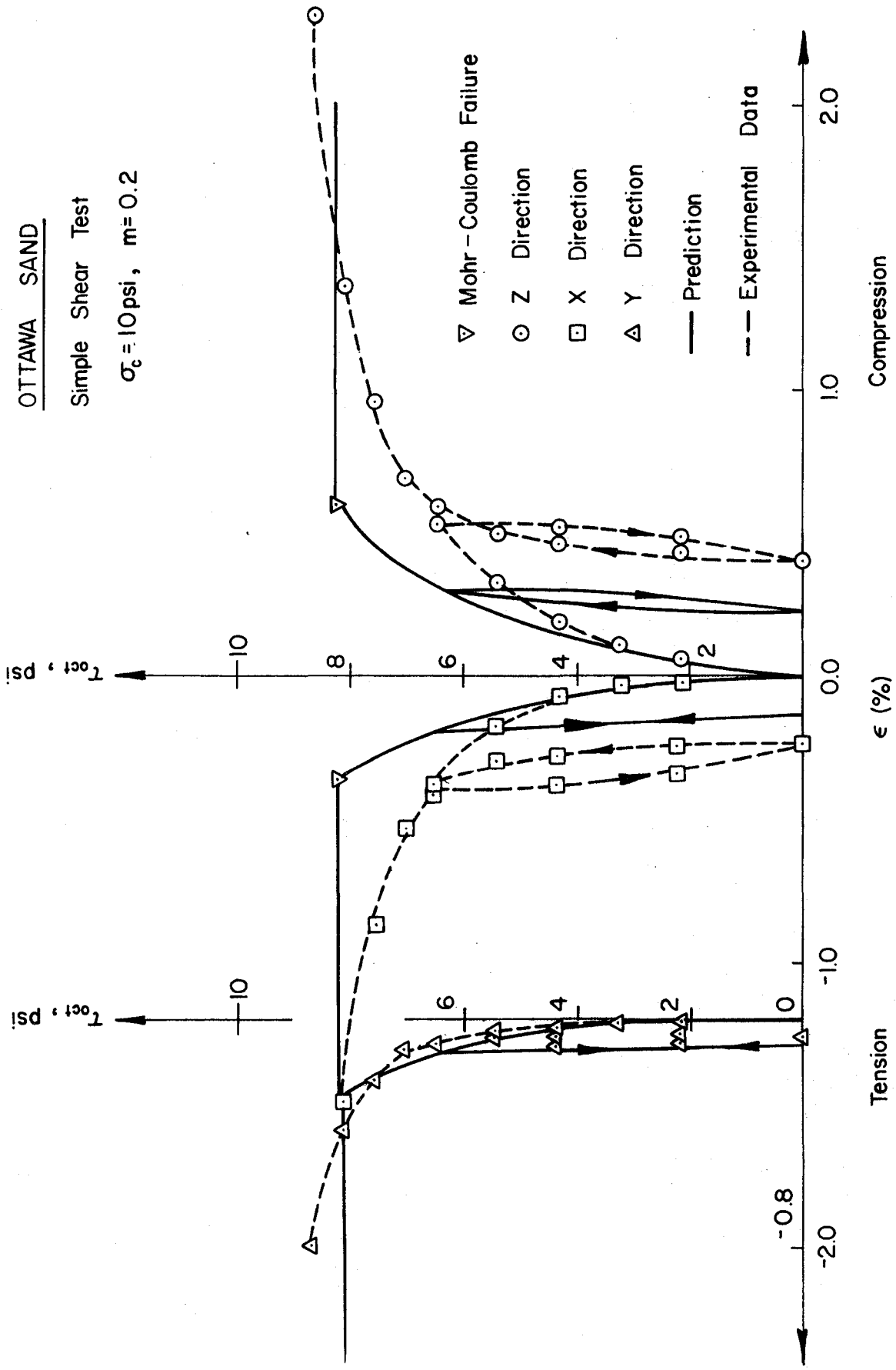

Fig. 13 Stress-Strain Relations for Ottawa Sand, Simple Shear Test (σ_c = 10 psi, m = 0.2)

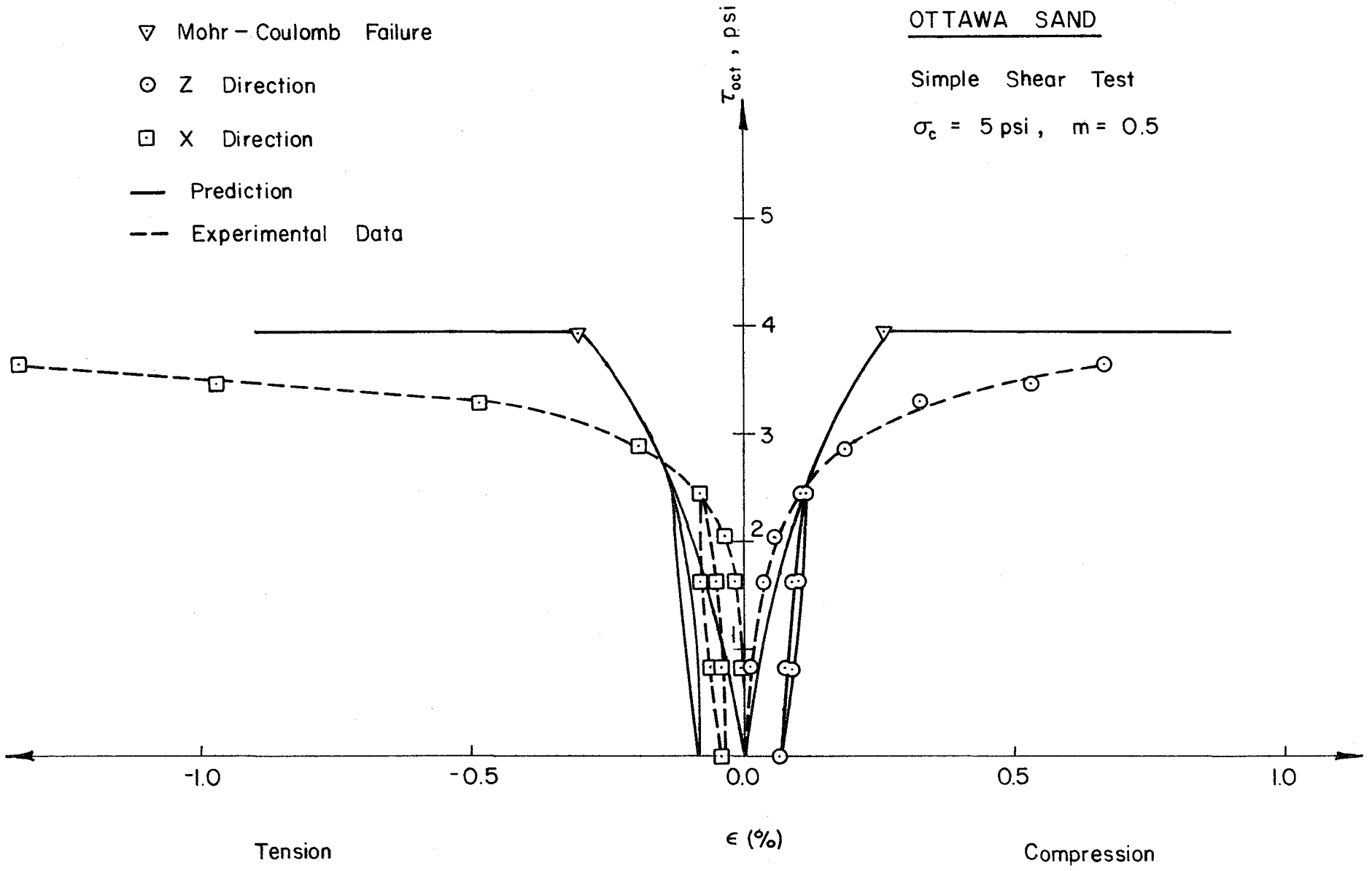

Fig. 14 Stress-Strain Relations for Ottawa Sand, Simple Shear Test (σ_c = 5 psi, m = 0.5)

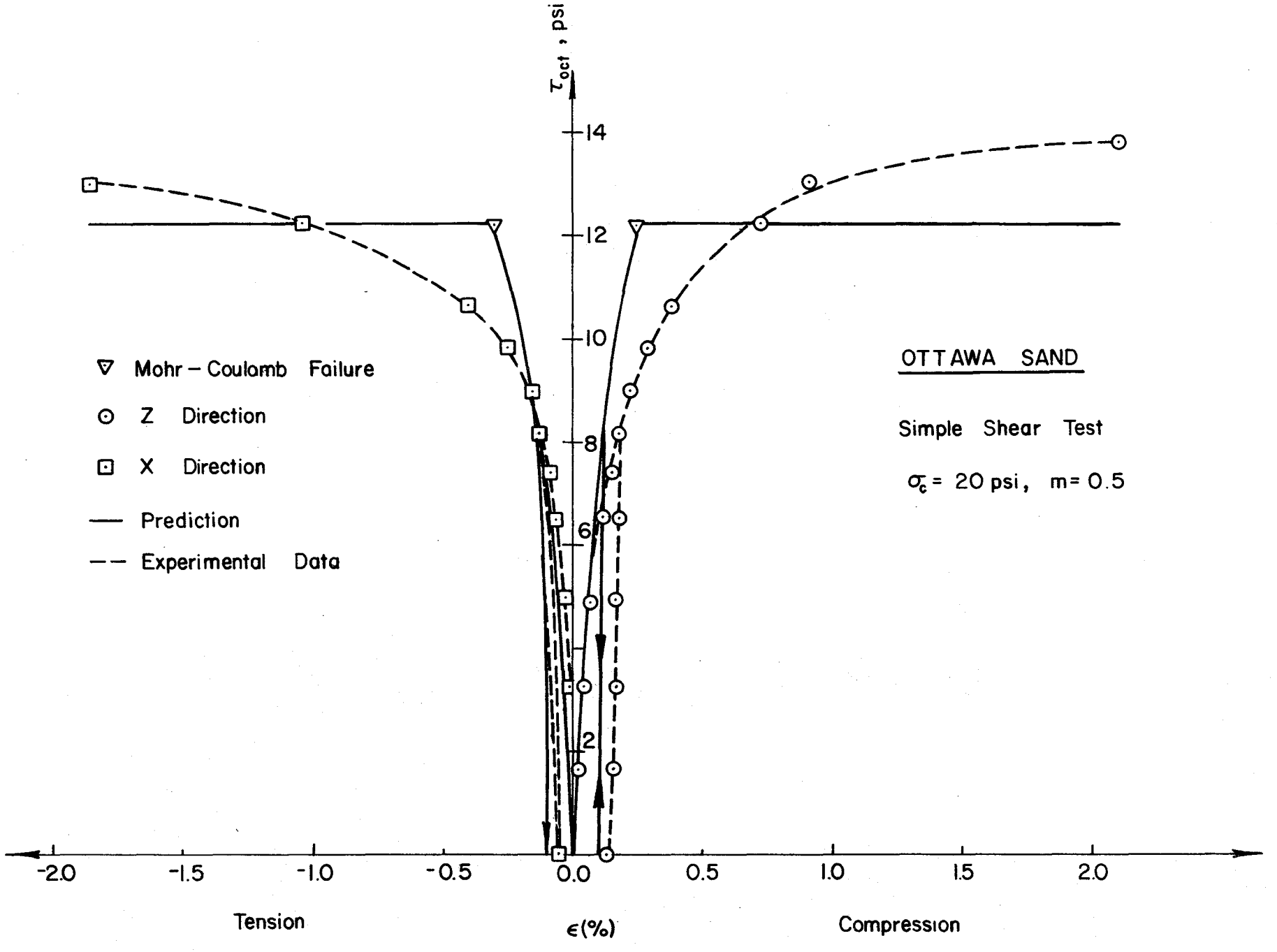

Fig. 15 Stress-Strain Relations for Ottawa Sand, Simple Shear Test (σ_c = 20 psi, m = 0.5)

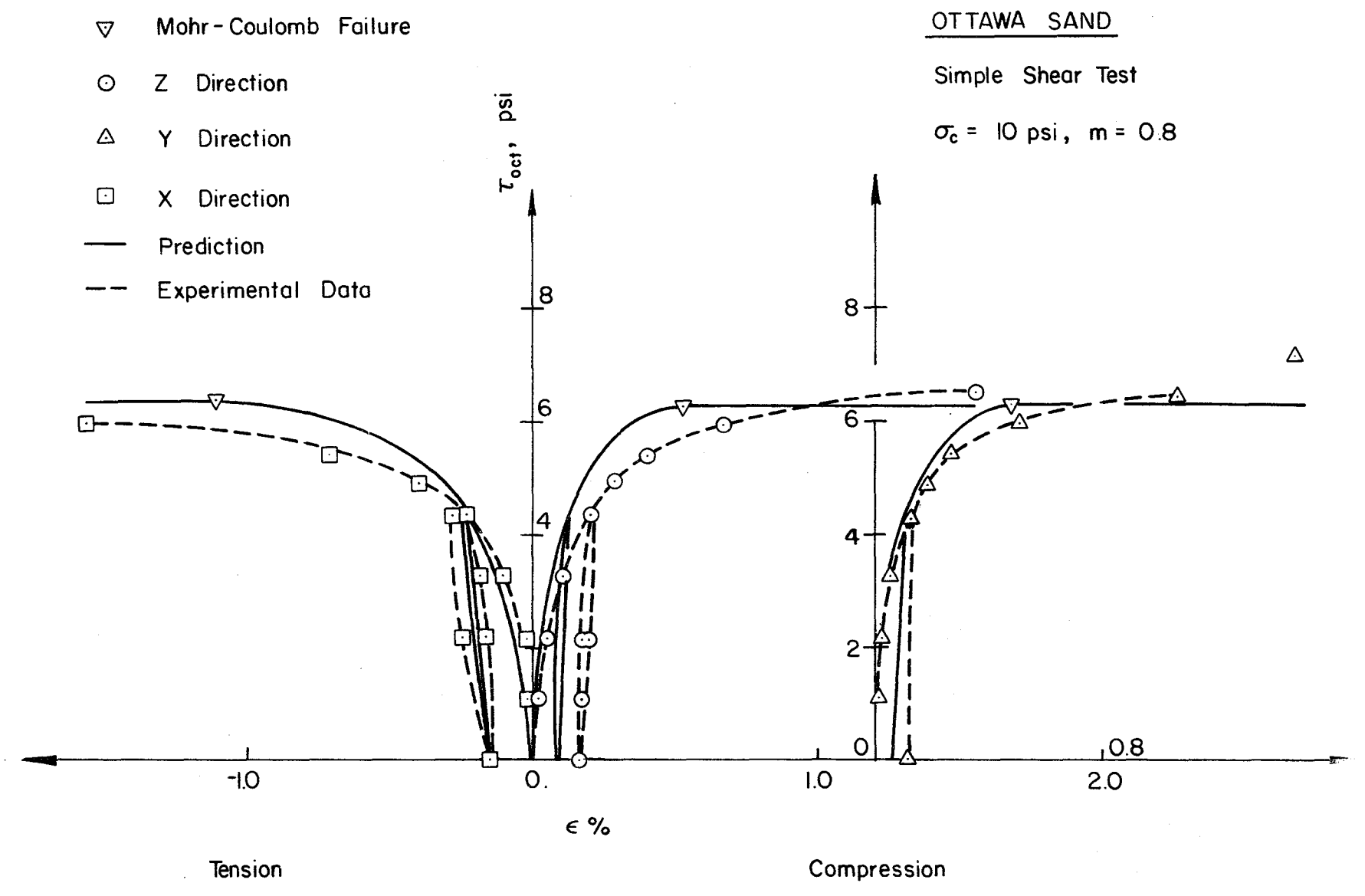

Fig. 16 Stress-strain Relations for Ottawa Sand, Simple Shear Test (σ_c = 10 psi, m = 0.8)

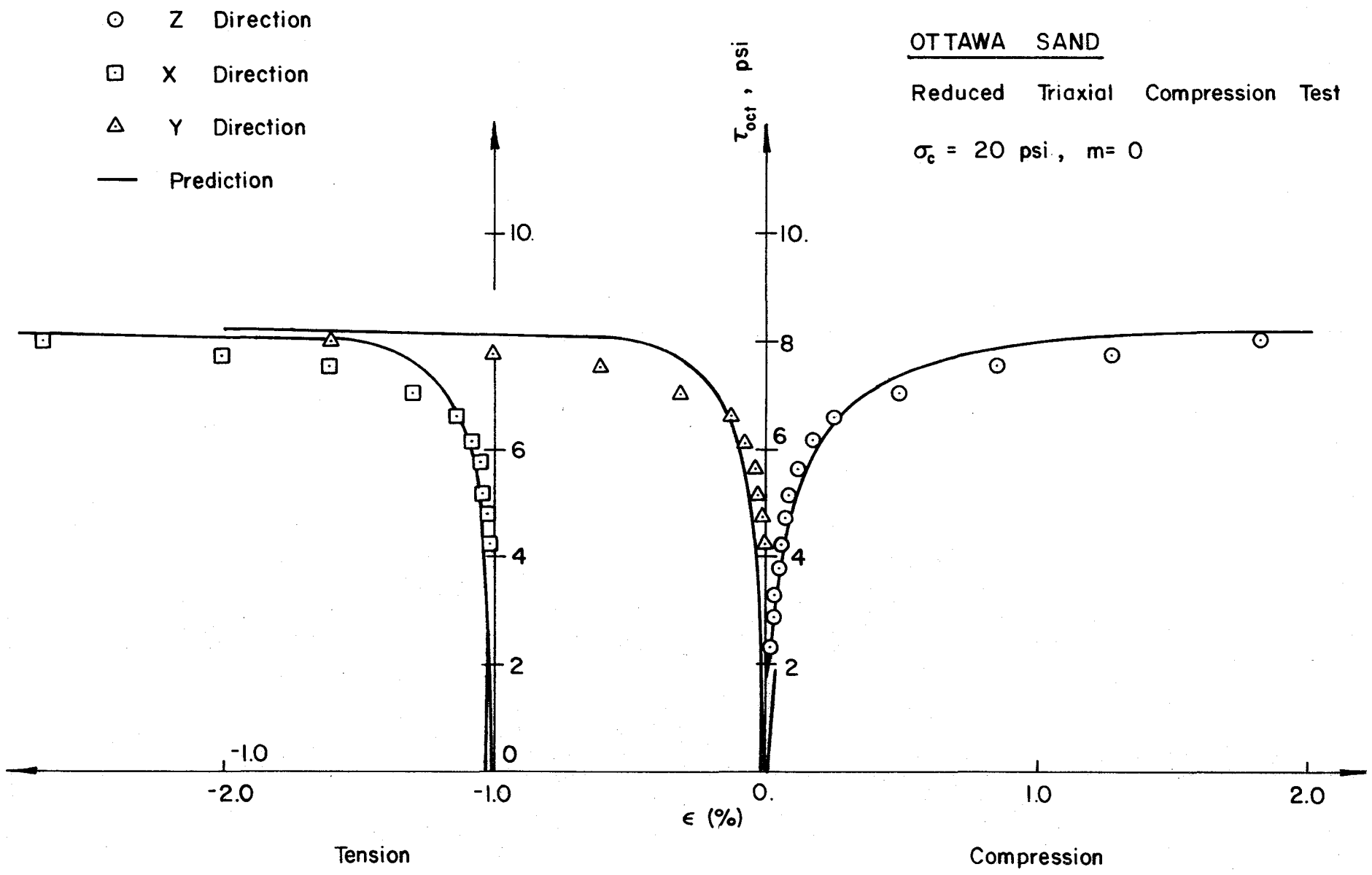

Fig. 17 Stress-Strain Relations for Ottawa Sand, RTC Test (σ_c = 20 psi, m = 0)

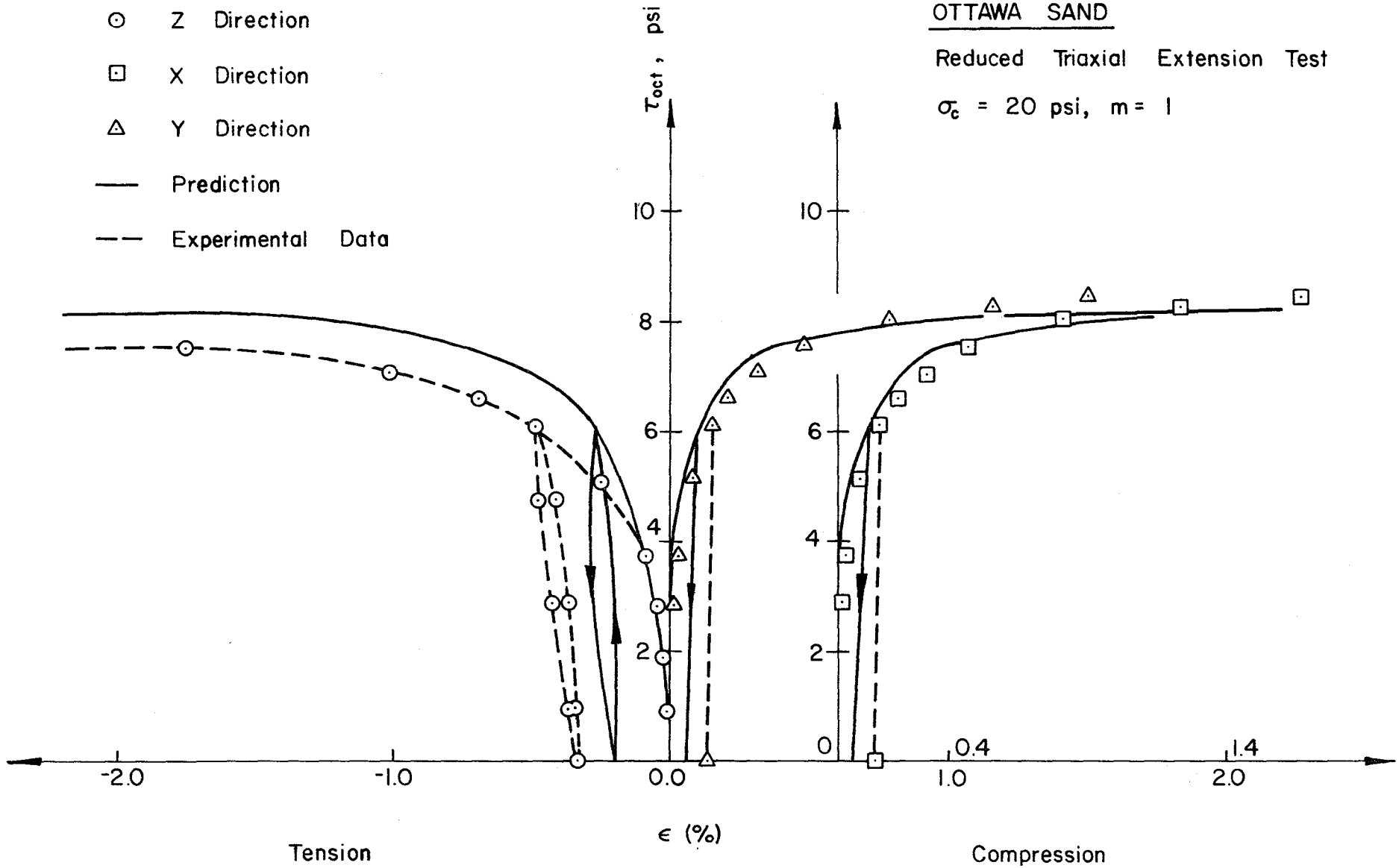

Fig. 18 Stress-Strain Relations for Ottawa Sand, RTE Test (σ_c = 20 psi, m = 1)

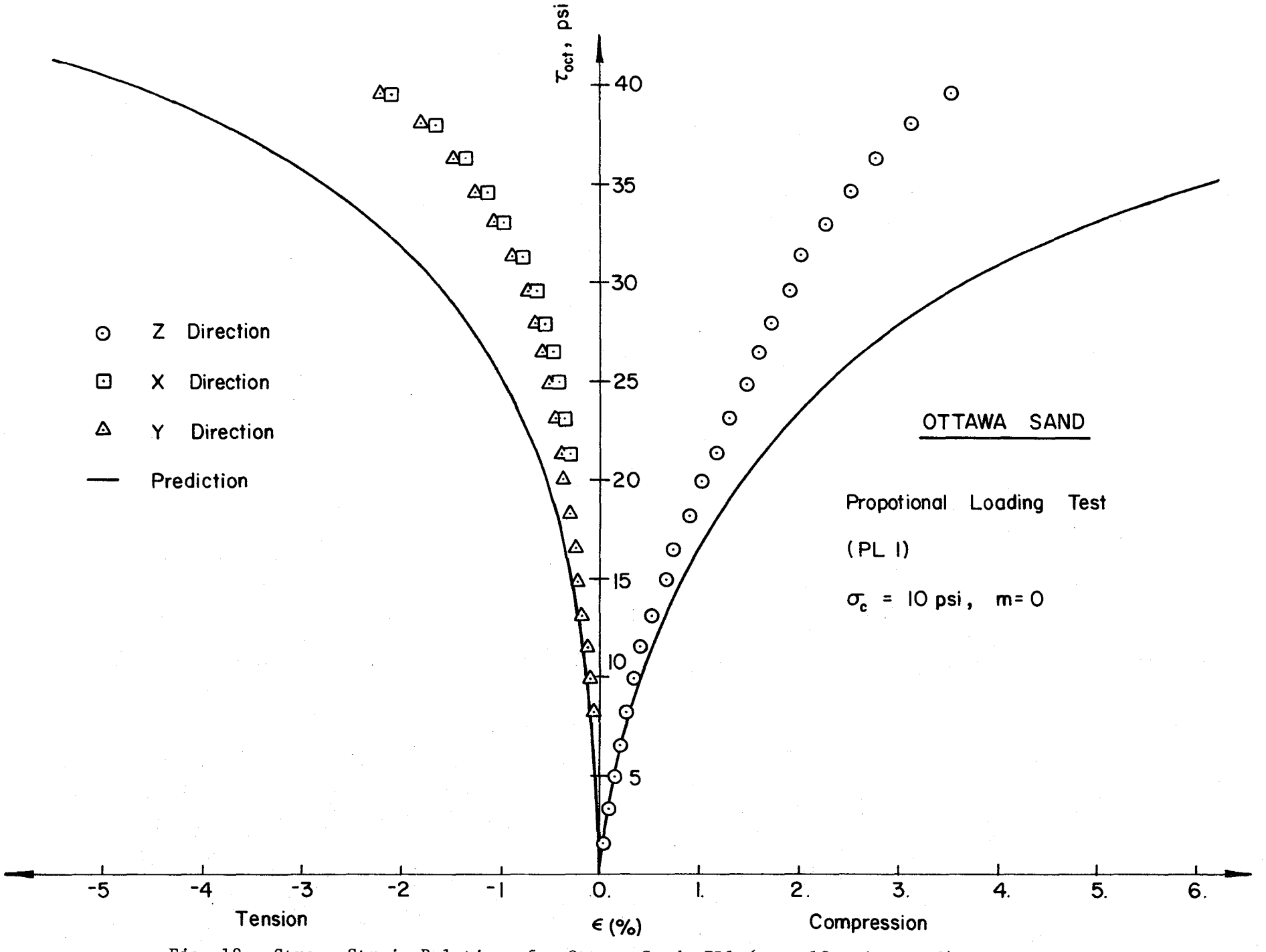

Fig. 19 Stress-Strain Relations for Ottawa Sand, PL1 (σ_c = 10 psi, m = 0)

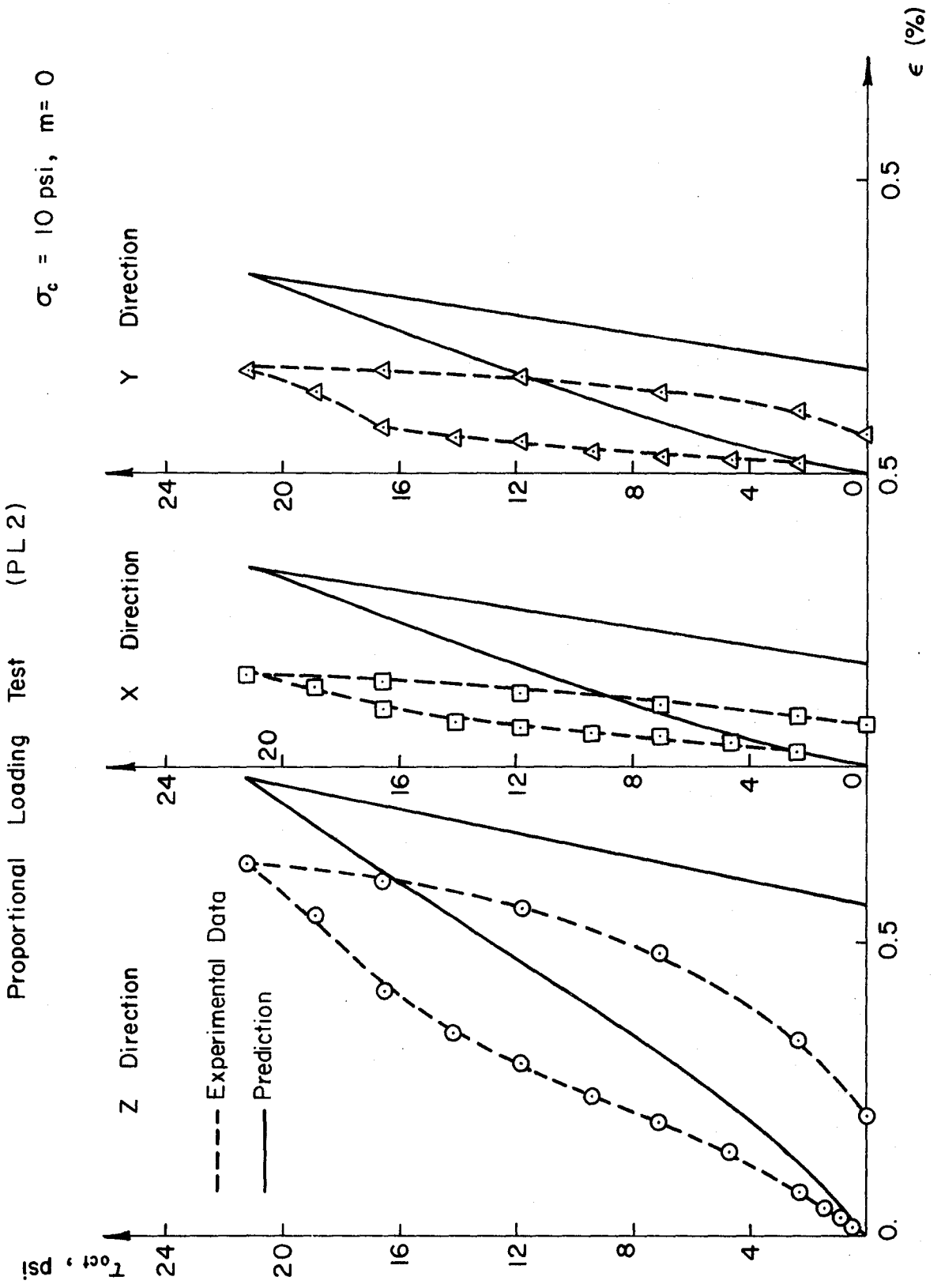

Fig. 20 Stress-Strain Relations for Ottawa Sand, PL2 (σ_c = 10 psi, m = 0)

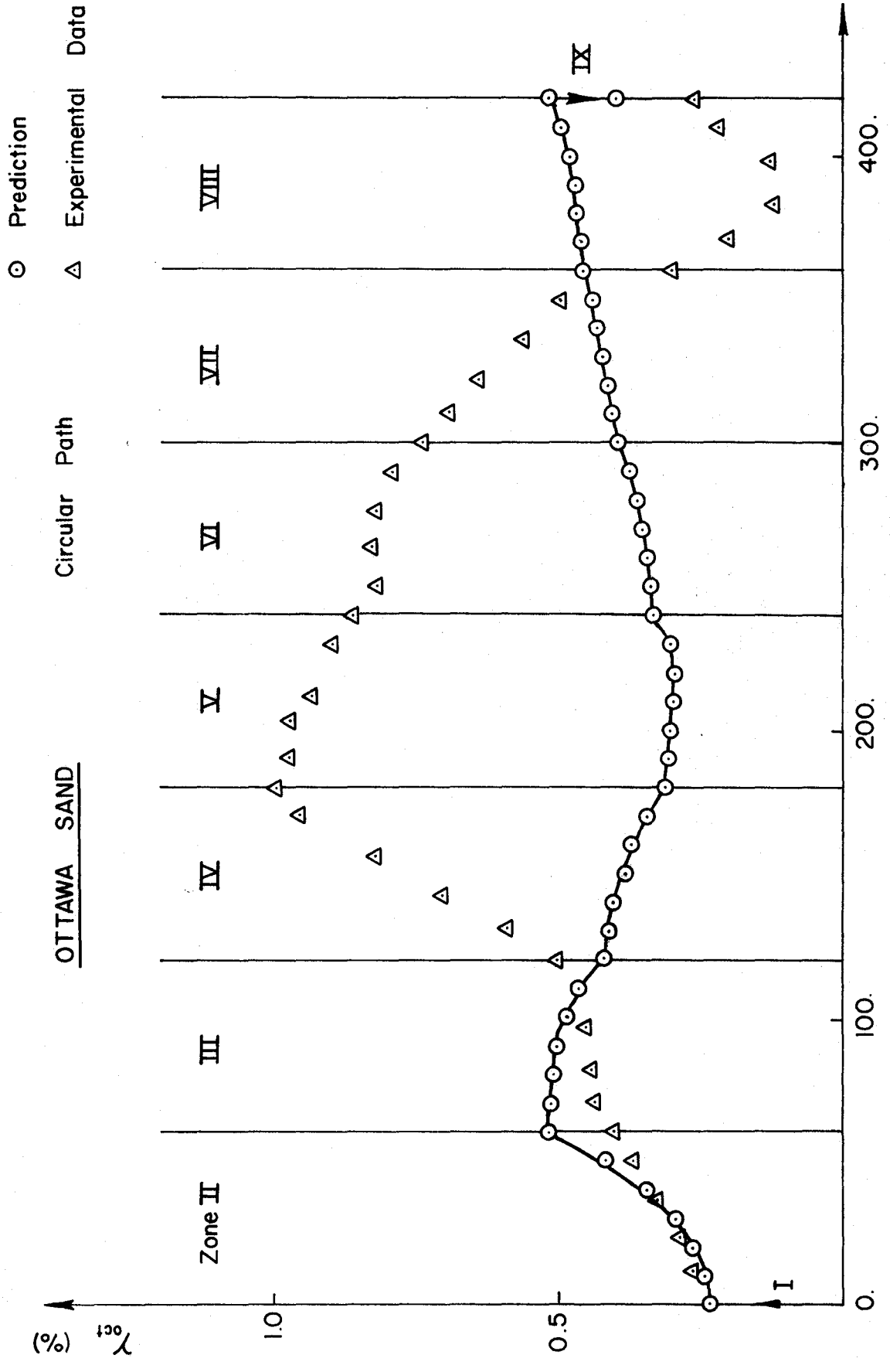

Fig. 21 Strain-Degree Relation for Ottawa Sand, Circular Path